Draft version August 28, 2023
Preprint typeset using LaTeX style emulateapj v. 01/23/15

THE RELATIONSHIP BETWEEN IGM Lyα OPACITY AND GALAXY DENSITY NEAR THE END OF REIONIZATION

Holly M. Christenson[1], George D. Becker[1], Anson D'Aloisio[1],Frederick B. Davies[3], Yongda Zhu[1], Elisa Boera[4], Fahad Nasir[3], Steven R. Furlanetto[2], Matthew A. Malkan[2]

Draft version August 28, 2023

ABSTRACT

Observed scatter in the Lyα opacity of quasar sightlines at $z < 6$ has motivated measurements of the correlation between Lyα opacity and galaxy density, as models that predict this scatter make strong and sometimes opposite predictions for how they should be related. Our previous work associated two highly opaque Lyα troughs at $z \sim 5.7$ with a deficit of Lyman-α emitting galaxies (LAEs). In this work, we survey two of the most highly transmissive lines of sight at this redshift, towards the $z = 6.02$ quasar SDSS J1306+0356 and the $z = 6.17$ quasar PSO J359-06. We find that both fields are underdense in LAEs within 10 h^{-1} Mpc of the quasar sightline, somewhat less extensive than underdensities associated with Lyα troughs. We combine our observations with three additional fields from the literature, and find that while fields with extreme opacities are generally underdense, moderate opacities span a wider density range. The results at high opacities are consistent with models that invoke UV background fluctuations and/or late reionization to explain the observed scatter in IGM Lyα opacities. There is tension at low opacities, however, as the models tend to associate lower IGM Lyα opacities with higher densities. Although the number of fields surveyed is still small, the low-opacity results may support a scenario in which the ionizing background in low-density regions increases more rapidly than some models suggest after becoming ionized. Elevated gas temperatures from recent reionization may also be making these regions more transparent.

Keywords: Reionization, Galaxies: Intergalactic Medium - High Redshift, Quasars: Absorption Lines

1. INTRODUCTION

Understanding when and how cosmic hydrogen reionization proceeded is of great interest for several reasons. First, the timing and duration of reionization have implications for our understanding of the first luminous sources. Second, our understanding of the physical state of the IGM is important context for high-redshift observations that are affected by absorption by intervening material. Lastly, reionization functions as a test of our dark matter and galaxy formation models, which must produce sources consistent with reionization constraints. There are two primary open questions that current reionization studies are attempting to address: the timing of reionization, including when it ended, and what the main sources of ionizing photons are (see Wise 2019 for a review).

A number of observations suggest that much of reionization took place between z$\sim 6-8$. Damping wings in quasar spectra at $z \geq 7$ suggest that the IGM is still substantially neutral at those redshifts (Mortlock et al. 2011; Greig et al. 2017; Bañados et al. 2018; Greig et al. 2019; Davies et al. 2018b; Wang et al. 2020). Galaxy surveys infer that a large portion of the universe remains neutral at $z \sim 7-8$ from the fraction of UV-selected galaxies that display Lyα emission (Mason et al. 2018; Jung et al. 2020; Morales et al. 2021). Measurements of the cosmic microwave background suggest a midpoint at $z \simeq 8$ (Planck Collaboration et al. 2020). The thermal history of the IGM down to $z \sim 5$ also suggests that much of reionization occurred at $z \sim 7$–8. (Boera et al. 2019; Gaikwad et al. 2020)

Until recently, reionization was thought to be essentially complete by $z \sim 6$ due to the observed onset of Lyα transmission in quasar spectra (Fan et al. 2006). On the other hand, a large scatter in Lyα opacity has been observed in quasar sightlines at $z \leq 6$ (Fan et al. 2006; Becker et al. 2015; Bosman et al. 2018; Eilers et al. 2018; Yang et al. 2020; Bosman et al. 2021; Zhu et al. 2021; Zhu et al. 2022). The Lyα forest at these redshifts exhibits highly opaque Lyα and Lyβ "troughs" down to $z \simeq 5.3$, the most extreme example of which is a 110 h^{-1} Mpc Lyα trough observed towards ULAS J0148+0600 (Becker et al. 2015). Both these troughs and the overall scatter in Lyα opacity have been shown to be inconsistent with a fully reionized IGM in which the ultraviolet background (UVB) is homogeneous (Becker et al. 2015; Bosman et al. 2018; Eilers et al. 2018; Yang et al. 2020; Bosman et al. 2021; Zhu et al. 2021; Zhu et al. 2022, see also Lidz et al. 2006).

The scatter in Lyα opacity and the presence of highly opaque sightlines such as that towards ULAS J0148+0600 suggests that there are large-scale variations

[1] Department of Physics Astronomy, University of California, Riverside, CA 92521, USA; hchri004@ucr.edu
[2] Department of Physics and Astronomy, University of California, Los Angeles, CA 90095, USA
[3] Max Planck Institut für Astronomie, Heidelberg, Germany
[4] INAF — Osservatorio Astronomico di Trieste, Trieste, Italy

in the hydrogen neutral fraction at these redshifts. For an ionized IGM, the neutral hydrogen fraction is set by the photoionization rate, the gas temperature, and the total hydrogen density, which broadly suggests multiple scenarios. The first is that large-scale fluctuations in the UVB are the primary cause of the scatter in Lyα opacity (Davies & Furlanetto 2016; Nasir & D'Aloisio 2020). In this scenario, we would qualitatively expect a transmissive sightline to span a high-density region, in close proximity to ionizing sources. In contrast, opaque sightlines would more typically be associated with voids. The second is that the scatter in Lyα opacity is primarily driven by large-scale fluctuations in temperature (D'Aloisio et al. 2015). In this scenario, a transmissive region would be underdense, recently reionized, and hot, whereas an opaque region would have been reionized early due to its high density of ionizing sources and able to cool for longer, producing a higher recombination rate. Lastly, it is possible that reionization is still ongoing at $z < 6$ and highly opaque troughs like that towards ULAS J0148+0600 correspond to islands of neutral hydrogen that have not yet been reionized (Kulkarni et al. 2019; Keating et al. 2020a; Nasir & D'Aloisio 2020). This "ultra-late" reionization scenario is not mutually exclusive with the other factors; fluctuations in the UVB and temperature would still be expected.

There are a number of models that make use of these physical processes to explain the observed scatter in Lyα opacity. Notably, the predictions they make for the relationship between opacity and density can be tested with observations. Fluctuating UVB models have been considered by numerous authors, and there are galaxy-driven variations (Davies & Furlanetto 2016; Nasir & D'Aloisio 2020) and quasar-driven variations (Chardin et al. 2015, 2017). We note that because quasars are rare, in quasar-driven UVB models the Lyα opacity is less tightly coupled to density than it is in galaxy-driven UVB models. The quasar-driven model is independently disfavored because the observed number density of quasars is not high enough to produce the required number of ionizing photons for quasars to be the main sources driving reionization (McGreer et al. 2018; Kulkarni et al. 2019; Faisst et al. 2022). Additionally, a quasar-driven hydrogen reionization may be incompatible with current constraints on helium reionization (D'Aloisio et al. 2017; McGreer et al. 2018; Garaldi et al. 2019). Similarly, the temperature model (D'Aloisio et al. 2015) is disfavored, at least as an explanation for the full range of opacities, by the observations of Becker et al. (2018), Kashino et al. (2020), Christenson et al. (2021), and Ishimoto et al. (2022), who found that highly opaque quasar sightlines are associated with galaxy underdensities. The late reionization models commonly include UVB fluctuations, but are distinct from pure UVB models in that regions of the IGM are still significantly neutral below $z = 6$. In these models, some highly opaque quasar sightlines correspond to neutral islands (Keating et al. 2020b). On the other hand, Nasir & D'Aloisio (2020) find that transmissive sightlines span a range of galaxy densities, but tend towards higher values. However, $\sim 10 - 15\%$ of transmissive sightlines in those models correspond to galaxy underdensities. Keating et al. (2020b) argue that sightlines where high transmission is correlated with galaxy underdensity should correspond to regions that are hot and recently reionized.

Observations spanning a range of Lyα opacity is necessary to robustly test the predictions from these reionization models and characterize the $z \sim 5.7$ opacity-density relationship. Previous studies have linked highly opaque quasar sightlines to galaxy underdensities towards the quasars ULAS J0148+0600 (Becker et al. 2018; Kashino et al. 2020; Christenson et al. 2021),SDSS J1250+3130 (Christenson et al. 2021), and SDSS J1630+4012 (Ishimoto et al. 2022). Ishimoto et al. (2022) also observe two sightlines of lower opacity, SDSS J1137+3549 and SDSS J1602+4228, and find that they correspond to galaxy overdensities.

In this paper, we extend our observations to some of the most highly transmissive sightlines known at these redshifts. We characterize the density of Lyman-α emitting galaxies (LAEs) towards the quasars SDSS J1306+0356, which has a Lyα effective opacity of $\tau_{\rm eff} = 2.6$, and PSO J359-06, which has a Lyα effective opacity of $\tau_{\rm eff} = 2.7$, both measured over 50 h^{-1} Mpc windows centered at $z = 5.7$, the redshift at which we select LAEs. We additionally include new selections of LAEs in the J0148 and J1250 fields, previously published in Becker et al. (2018); Christenson et al. (2021) to make comparisons between the four fields as self-consistent as possible. We summarize the observations in Section 2, and describe the photometry and LAE selection criteria in Section 3. We present the results of LAE selections in Section 4, and compare the results to predictions from current models in Section 5 before summarizing in Section 6. Throughout this work, we assume a ΛCDM cosmology with $\Omega_m = 0.3$, $\Omega_\Lambda = 0.7$, and $\Omega_b = 0.048$. All distances are given in comoving units, and all magnitudes are in the AB system.

2. OBSERVATIONS

2.1. *QSO Spectra*

Table 1
Effective opacity measurements for QSO sightlines referenced in this work

QSO	z_{QSO}	$\tau_{\rm eff}^{50,a}$	$\tau_{\rm eff}^{28,b}$
ULAS J0148+0600	5.998	7.573^c	7.329^c
SDSS J1250+3130	6.137	5.876^c	5.610^c
SDSS J1306+0356	6.0330	2.662 ± 0.009	2.475 ± 0.010
PSO J359-06	6.1718	2.680 ± 0.009	2.392 ± 0.009
SDSS J1602+4228[d]	6.079	3.063 ± 0.038	4.898 ± 0.308
SDSS J1137+3549[d]	6.007	2.904 ± 0.040	4.344 ± 0.227
SDSS J1630+4012[d]	6.055[e]	3.857 ± 0.184	4.550 ± 0.477

[a] Effective opacity measured over a 50 h^{-1} Mpc window centered at 8177 Å
[b] Effective opacity measured over the FWHM of the $NB816$ filter (a 28 h^{-1} Mpc window) centered at 8177 Å
[c] Lower limit
[d] From Ishimoto et al. (2022); see Section 5.3 for a detailed discussion of these sightlines
[e] Redshift measurement from Becker et al. (2019).

The four sightlines whose fields we survey in this work were drawn from the sample of Zhu et al. (2021). This sample includes spectra of 55 quasars over $5.5 \leq z \leq 6.5$ taken with the X-Shooter spectrograph on the Very

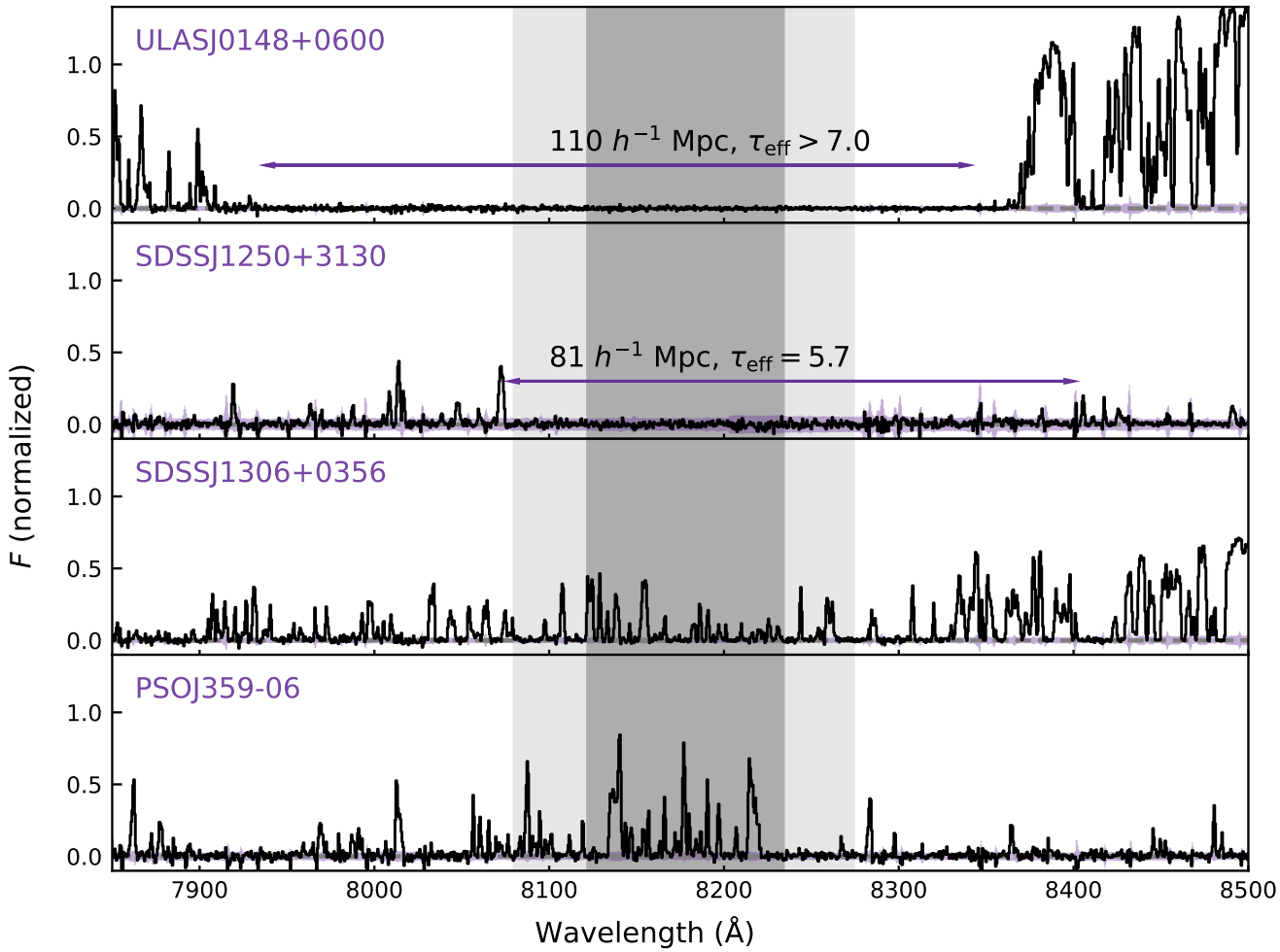

Figure 1. Partial spectra of the Lyα forest of quasars ULAS J0148+0600 (X-Shooter), SDSS J1250+3130 (Keck/ESI), SDSS J1306+0356 (X-Shooter), and PSO J359-06 (X-Shooter), whose fields we observe with Subaru/HSC. The J0148 and J1250 sightlines have $\tau_{\rm eff} \geq 7.0$ and $\tau_{\rm eff} = 5.7 \pm 0.4$ measured over 110 and 81 h^{-1} Mpc respectively (trough extent marked with purple arrows). The shaded purple regions indicate the $\pm 1\sigma$ uncertainty interval. The darker shaded gray rectangles indicates the FWHM of the NB816 filter, and the lighter shaded regions indicate a 50 h^{-1} Mpc interval, both centered at 8177 Å; these windows are used to calculate the effective opacity of the sightlines. The effective opacity measurements are summarized in Table 1. These spectra are normalized using PCA fits to their continuum. Note that for the J0148 spectrum, flux at $\lambda > 8350$ Å is part of the quasar proximity zone and not fully normalized.

Large Telescope and the Echellete Spectrograph and Imager on Keck, 23 of which are from the XQR-30 VLT Large Programme. Subsets of the four quasar spectra are shown in Figure 1, displaying the highly opaque troughs (J0148 and J1250) and the highly transmissive regions (J1306 and J359) near $z = 5.7$ found in these sightlines (Becker et al. 2015, 2019; Zhu et al. 2021). The J1306 sightline has an effective opacity of $\tau_{\rm eff}^{50} = 2.617 \pm 0.009$, where $\tau_{\rm eff} = -\ln\langle\ F\ \rangle$ and F is the mean continuum-normalized flux. The J359 sightline has an effective opacity of $\tau_{\rm eff}^{50} = 2.661 \pm 0.009$. For both sightlines, $\tau_{\rm eff}^{50}$ is measured over 50 h^{-1} Mpc windows centered at $z = 5.7$ (8177 Å), which cover $5.632 < z < 5.794$. These two sightlines are some of the most highly transmissive sightlines known at these redshifts (Zhu et al. 2021). Similarly, the J0148 and J1250 are two of the most highly opaque sightlines observed at these redshifts, with large troughs of $\tau_{\rm eff} \geq 7$ measured over 110 h^{-1} Mpc and $\tau_{\rm eff} \geq 5.7 \pm 0.4$ measured over 81 h^{-1} Mpc respectively. Over 50 h^{-1} Mpc windows centered at 8177Å, the sightlines have $\tau_{\rm eff}^{50} \geq 7.0$ and $\tau_{\rm eff}^{50} = 5.03 \pm 0.21$ respectively. We also calculate $\tau_{\rm eff}$ for these sightlines over a 28 h^{-1} Mpc window, which represents the full width at half maximum of the narrow-band filter used for LAE selection, and find $\tau_{\rm eff}^{28} \geq 7.329$ for the J0148 sightline, $\tau_{\rm eff} \geq 5.610$ for the J1250 sightline, $\tau_{\rm eff} = 2.475 \pm 0.010$ for the J1306 sightline, and $\tau_{\rm eff} = 2.392 \pm 0.009$ for the J359 sightline. For all of the effective opacity measurements, we adopt a lower limit of $\tau_{\rm eff} \geq -\ln(2\sigma_{\langle F \rangle})$ if the mean flux is negative or detected with less than 2σ significance. This definition is consistent with previous works (e.g., Eilers et al. 2018). The opacity measurements used in this work are summarized in Table 1. We estimate Lyα opacity for these sightlines using our imaging data in Appendix A.

2.2. *HSC Imaging*

Presented here for the first time are imaging data in the J1306 and J359 fields, taken with Subaru Hyper Suprime Cam (HSC). This work also makes use of HSC imaging in the J0148 and J1250 fields, previously presented in

Becker et al. (2018) and Christenson et al. (2021). Observations of the J1306 field were made via the HSC queue in April and June 2019, May 2020, and January and June 2021. Observations of the J359 field were made via the HSC queue in October and November 2019, August 2020, and November 2021. All observations in these fields were made during dark time. As for previous fields surveyed in this program, images were centered at the quasar position. This program makes use of two HSC broadband filters, $r2$ and $i2$, and the narrowband $NB816$ filter, which has a transmission-averaged mean wavelength $\lambda = 8168$ Å and $\geq 50\%$ transmission over 8122 Å$\leq \lambda \leq$ 8239 Å. The wavelength coverage of the $NB816$ filter coincides with the Lyα line at $z \sim 5.7$.

Table 2
Summary of HSC imaging

	Filter	t_{exp} (hrs)	Seeing[a]	$m^b_{50\%>5\sigma}$	$m^c_{5\sigma,1.2''}$
J0148	$r2$	1.5	0.61	26.3	26.2
	$i2$	2.4	0.71	25.9	25.8
	$NB816$	4.5	0.60	25.1	25.2
J1250	$r2$	2.0[d]	1.07	26.3	26.2
	$i2$	2.5	0.62	26.1	26.0
	$NB816$	2.8	0.73	25.1	25.2
J1306	$r2$	1.3	0.89	26.3	26.2
	$i2$	2.4	0.74	26.1	26.0
	$NB816$	2.8	0.80	25.0	25.1
J359	$r2$	1.5	1.08	26.2	26.3
	$i2$	1.9	0.73	25.8	25.9
	$NB816$	2.2	0.87	25.0	25.2

[a] Median seeing FWHM in combined mosaic.
[b] Magnitude at which 50% of detected sources have $S/N \geq 5$ in the corresponding filter.
[c] Limiting magnitude, given by five times the standard deviation of the flux measured in empty 1.5″ apertures.
[d] Partially observed during gray time.

The observations in all four fields are summarized in Table 2, as well as the image depth measured in empty 1.2″ apertures and the median 5σ limiting aperture magnitudes in each band. At the limiting magnitudes, at least 50% of the detected sources have a signal-to-noise ratio $S/N_{NB816} \geq 5$.

We used version 21 of the LSST Science Pipeline (Ivezić et al. 2008; Jurić et al. 2015) to reduce individual CCDs and combine them into stacked mosaics. The pipeline uses PanStarrs DR1 imaging (Chambers et al. 2016) for photometric calibrations. We used Source Extractor (Bertin & Arnouts 1996) to create a catalog of NB816-detected sources and their spatial coordinates in the stacked mosaics, and then make our own photometric measurements at these coordinates, as described below.

3. METHODS

3.1. *Photometry*

The LAE selection in this work makes use of aperture fluxes as the primary photometric measurement. This choice is a departure from our previous work, which was based on PSF (Christenson et al. 2021) or CModel fluxes (Becker et al. 2018). As we discuss further in Section 5, a major focus of this paper is comparing the fields to one another, which requires minimizing the effect of variations in depth, seeing, and completeness. While PSF fluxes can be optimized for the detection of faint and unresolved sources, aperture fluxes are less easily impacted by small changes in the seeing and more robust for resolved sources. We have therefore opted to accept a lower signal-to-noise ratio and the loss of some faint LAEs from our catalog in favor of a more robust selection.

The source detection and photometric measurements are carried out via the following steps. Source positions are identified in the NB816 stacked mosaic using Source Extractor. At each source position, we measure the flux in a 1.5″ aperture, and also measure the sky background in a $1.5 - 5''$ annulus around the aperture, excluding pixels labeled as sources by the LSST pipeline. The aperture fluxes are corrected by the measured sky background. These measurements are made independently, at the same position, in each band.

3.2. *LAE selection procedure*

Our selection criteria, following Christenson et al. (2021), are based on those of Ouchi et al. (2008). As noted in Christenson et al. (2021), our observations have some disparity in depth between different bands and fields. To ensure a high-quality selection of LAEs, we impose additional requirements that are designed to exclude objects with large uncertainties in their colors. The selection criteria are as follows:

- $NB \leq 25.5$
- $S/N_{NB816} \geq 5.0$
- $\frac{F_{NB816}}{F_{i2}} \geq 3.0$ (50% probability) and $\frac{F_{NB816}}{F_{i2}} \geq 1.7$ (95% probability)
- $F_{r2} \leq 2\sigma_{r2}$, or $F_{r2} \geq 2\sigma_{r2}$ and $F_{i2}/F_{r2} \geq 2.5$
- $\frac{F_{NB816}}{F_{r2}} \geq 7.6$ (50% probability) and $\frac{F_{NB816}}{F_{r2}} \geq 4.0$ (95% probability)

The 95% probability thresholds are the lower bound of the 1σ error of an object with $F_{NB816}/F_{i2} = 3.0$, $F_{i2}/F_{r2} = 2.5$, and $S/N_{NB816} = 5.0$. All objects that satisfy these requirements undergo a visual inspection to remove spurious sources, such as satellite trails. Examples of selected LAEs are shown in Figure 2.

3.3. *Completeness Corrections*

We make completeness corrections for the selected catalog of LAEs in two stages. The first stage is to calculate a completeness correction in each field as a function of $NB816$ magnitude and distance from the quasar sightline. This calculation is based on artificially injected LAE candidates, which are placed at randomly generated positions in the field, binned by radius and magnitude, put through the LAE selection procedures described in Section 3. The sample is generated such that the artificial LAEs are spread roughly evenly between the magnitude and radius bins, ensuring that there are enough objects in each bin to calculate a completeness correction. The completeness correction is the reciprocal of the fraction of artificial LAEs that were successfully detected in each bin. We show the completeness measured in each field

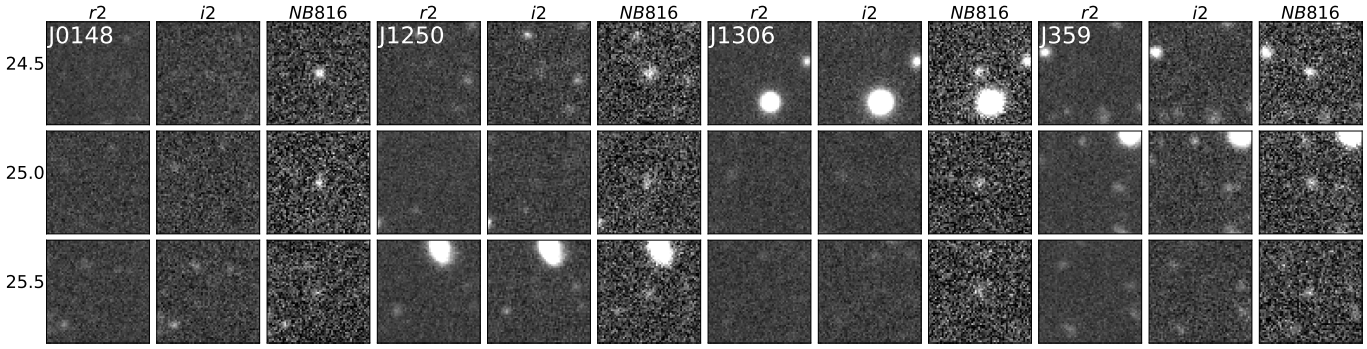

Figure 2. Example LAE candidates selected in all four fields with the criteria described in Section 3.2. The cutout images are 10 ″ on each side and centered on the LAE position. For each field, we show an example candidate selected to have NB816 = 24.5, 25.0, and 25.5 (top to bottom) in the $r2, i2$, and NB816 bands (left to right).

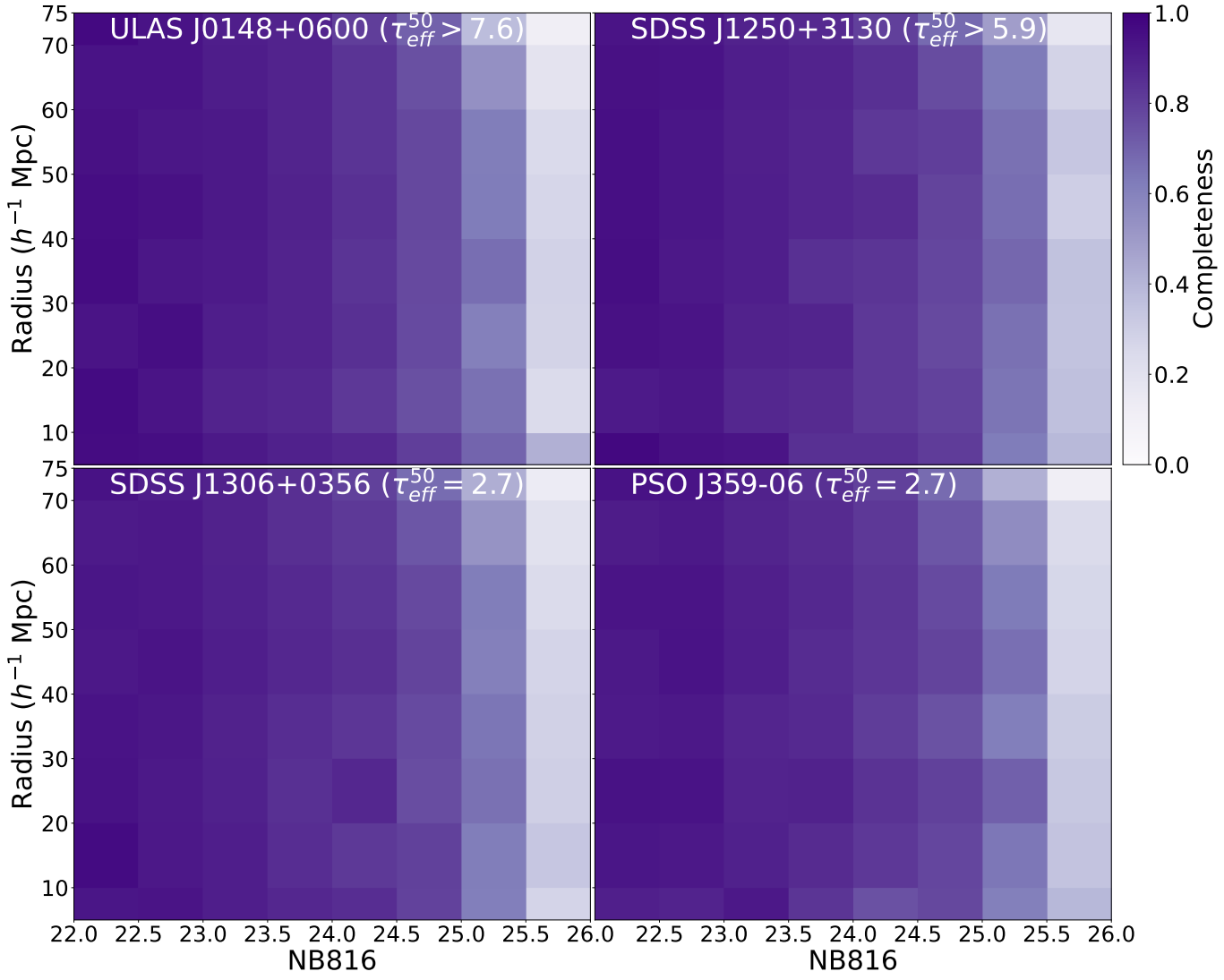

Figure 3. Completeness measured in the J0148 (top left), J1250 (top right), J1306 (bottom left) and J359 (bottom right) fields as a function of projected distance from the quasar position and $NB816$ magnitude. The completeness is given by the fraction of artificial LAEs injected into the imaging that were detected by our LAE selection procedure. Note that we have included narrowband magnitudes down to $NB816 = 26.0$; however, we only include sources down to $NB816 = 25.5$ due to the low completeness in the faintest magnitude bin.

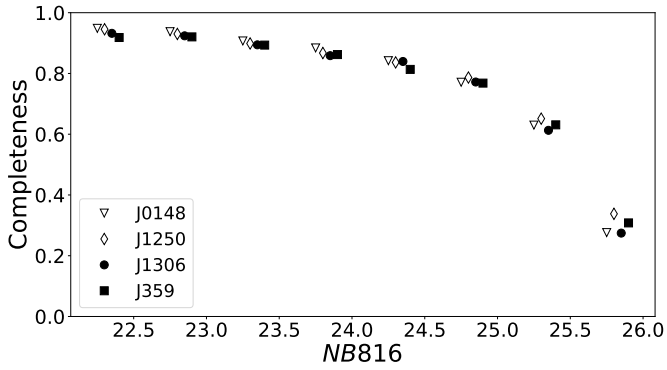

Figure 4. Radially averaged completeness measured in the J0148 (filled gray triangles), J1250 (open gray diamonds), J1306 (filled black circles), and J359 (open black squares) fields as a function of $NB816$ radius as a function of distance from the quasar position and $NB816$ magnitude. The fields are offset horizontally for clarity. While we have calculated the completeness for narrowband magnitudes down to $NB816 = 26.0$, our analysis only includes sources down to $NB816 = 25.5$.

as a function of distance from the quasar position and NB816 magnitude in Figure 3. The completeness calculations are made down to NB816 $\leq$ 26.0, but we only select LAEs to NB816 $\leq$ 25.5 in our final catalog because of the low completeness measured in the faintest magnitude bin. This completeness correction is used to correct the measured surface density as a function of radius and magnitude shown in Section 4 in Figures 5, 7, 10, and 11. We additionally show the radially averaged completeness as a function of $NB816$ magnitude in Figure 4.

The second stage is calculating total completeness as a function of position in each field. We use the completeness-corrected magnitude distribution of LAEs detected in all four fields to generate a second set of artificial LAEs in each field, this time with NB816 magnitudes drawn from the empirical magnitude distribution. Because these artificial LAEs are representative of the real LAE sample, we can use them to calculate a map of completeness as a function of position. We assign each artificial LAE a flag indicating whether or not it was successfully selected using our LAE selection procedure, and then calculate the surface density of both (i) the full artificial LAE catalog and (ii) the selected artificial LAEs in each field as a function of position. Surface densities are estimated using the kernel density estimation approach described below. The completeness as a function of position is then given by the surface density of the selected LAEs divided by the surface density of the injected LAEs. The completeness is fairly uniform, with variations of $\leq$ 10% on $\sim$ 5 h^{-1} Mpc scales, out to a radius of $\sim 40'$. At larger radii, the completeness declines sharply. We calculate these completeness correction maps separately for each field, and apply them to the LAE maps shown in Figure 6.

4. RESULTS

We select 298 LAEs in the J0148 field, 247 in the J1250 field, 192 in the J1306 field, and 228 in the J359 field using the procedures outlined in section 3. The number of LAEs selected in the J0148 and J1250 fields is somewhat lower than found in Christenson et al. (2021) due to the use of aperture fluxes, although the spatial distribution of the sources is qualitatively similar. We compare the

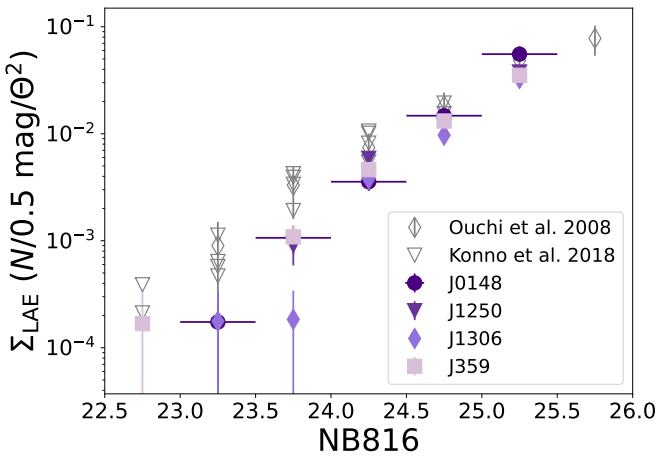

Figure 5. Completeness-corrected surface density of LAE candidates in the J0148, J1250, J1306, and J359 fields (filled markers) as a function of their $NB816$ magnitude (see Section 3.3 for details on the completeness correction.). The error bars on the completeness-corrected measurements are 68% Poisson intervals. We also show measurements from Konno et al. (2017) (open gray triangles, includes four HSC fields plotted separately) and Ouchi et al. (2008) (open gray diamonds) for comparison.

two selections in more detail in Appendix D. We show the completeness-corrected surface density of the LAE catalogs in each field as a function of their NB816 magnitude in Figure 5. Also included are measurements from Konno et al. (2017) and Ouchi et al. (2008). We note that we find a lower surface density of bright objects than reported in the literature. This difference arises from our use of 1.5″ apertures throughout, rather than using adaptively scaled apertures for the primary magnitude measurement as done in Ouchi et al. (2008). In some cases the 1.5″ apertures miss some of the flux in brighter, more extended objects.

Table 3
LAE number density as a function of radius

	R (Mpc)	N_{LAEs}	N^a_{corr}	Σ LAE (Mpc h^{-1})^{2,b}
J0148	5(0 – 10)	0	0	0.0 (0.0 – 0.0)
	15(10 – 20)	12	17	0.018 (0.013 – 0.022)
	25(20 – 30)	33	50	0.032 (0.028 – 0.036)
	35(30 – 40)	44	61	0.028 (0.024 – 0.031)
	45(40 – 50)	51	76	0.027 (0.024 – 0.03)
	55(50 – 60)	56	86	0.025 (0.022 – 0.027)
	65(60 – 70)	74	126	0.031 (0.028 – 0.034)
	72(70 – 74.5)	28	61	0.03 (0.026 – 0.034)
J1250	5(0 – 10)	2	3	0.01 (0.005 – 0.016)
	15(10 – 20)	9	12	0.013 (0.009 – 0.017)
	25(20 – 30)	21	29	0.019 (0.015 – 0.022)
	35(30 – 40)	32	44	0.02 (0.017 – 0.023)
	45(40 – 50)	37	52	0.018 (0.016 – 0.021)
	55(50 – 60)	61	87	0.025 (0.022 – 0.028)
	65(60 – 70)	63	94	0.023 (0.021 – 0.025)
	72(70 – 74.5)	22	37	0.018 (0.015 – 0.021)
J1306	5(0 – 10)	2	3	0.01 (0.005 – 0.016)
	15(10 – 20)	16	24	0.025 (0.02 – 0.031)
	25(20 – 30)	28	40	0.026 (0.022 – 0.029)
	35(30 – 40)	35	50	0.023 (0.02 – 0.026)
	45(40 – 50)	27	40	0.014 (0.012 – 0.016)
	55(50 – 60)	39	59	0.017 (0.015 – 0.019)
	65(60 – 70)	30	50	0.012 (0.01 – 0.014)
	72(70 – 74.5)	15	31	0.015 (0.013 – 0.018)
J359	5(0 – 10)	1	1	0.004 (0.002 – 0.006)
	15(10 – 20)	11	16	0.017 (0.012 – 0.021)

Table 3 — Continued

R (Mpc)	N_{LAEs}	N^a_{corr}	Σ LAE (Mpc h^{-1})^{2,b}
25(20 − 30)	22	29	0.019 (0.015 − 0.022)
35(30 − 40)	32	49	0.022 (0.019 − 0.025)
45(40 − 50)	34	48	0.017 (0.015 − 0.019)
55(50 − 60)	46	69	0.02 (0.018 − 0.023)
65(60 − 70)	57	89	0.022 (0.02 − 0.024)
72(70 − 74.5)	25	43	0.021 (0.018 − 0.024)

[a] Completeness corrected
[b] Ranges quoted in parentheses correspond to 68% Poisson intervals.

Figure 6 shows the distribution of LAE candidates in all four fields: J0148 (top left), J1250 (top right), J1306 (bottom left), and J359 (bottom right). In each panel, the field is centered on the quasar position, which is marked with a yellow star. The concentric dotted rings indicate 10 h^{-1} Mpc intervals from the quasar position, and the solid black ring indicates the edge of the field. The LAEs are represented with a color that indicates their NB816 magnitude. There are several bright foreground stars in these fields that obscure small portions of the field, which are masked out in white. The grayscale shading indicates the surface density of LAEs. To calculate the surface density, we overlay a grid of 0.24′ (0.4 h^{-1} Mpc) pixels on the field and then find the surface density in each grid cell by kernel density estimation using a Gaussian kernel with a 1.6′ bandwidth. This smoothing scale is chosen to match the mean separation between each LAE and its nearest neighbor. The surface density is then completeness-corrected as described in Section 3.3 and normalized by the mean surface density of the field over $15 \leq \theta \leq 40$ arcmin. See Appendix C for maps normalized using a global mean surface density, calculated over the $15 \leq \theta \leq 40$ arcmin region of all four fields.

Figure 7 shows the surface density of LAEs in each field as a function of distance from the quasar position. We first measure the raw surface density by binning the LAEs into 10 h^{-1} Mpc annuli, and then further bin them by NB816 magnitude to apply the completeness correction shown in Figure 3. The raw measurements are shown in Figure 7 with gray, open triangles, and the completeness-corrected measurements are shown with filled, black circles. The horizontal dotted line represents the mean completeness-corrected surface density of the field, which we measure over $15 \leq \theta \leq 40'$. The surface density measurements in each annular bin for the four fields are summarized in Table 3.

We find that all four fields in the survey are underdense within ~ 10 h^{-1} Mpc of the quasar sightline; all except the J1306 field are also underdense out to 20 h^{-1} Mpc. The J1306 field is mildly overdense between 10 and $\sim 30 - 40$ h^{-1} Mpc. This re-selection of LAEs in the J0148 and J1250 fields based on aperture photometry is consistent with our previous selections in Christenson et al. (2021) (J0148 and J1250) and Becker et al. (2018) (J0148), both in the large-scale structures reflected in the LAE distribution and in the association between highly opaque sightlines and galaxy underdensities. Additionally, we newly find an association between these two transmissive sightlines and galaxy underdensities within 10 h^{-1} Mpc.

5. ANALYSIS

5.1. *Comparison of radial distributions to model predictions*

We can compare the results of the LAE selection in these fields directly to the predictions made by various models. In this section, we consider only the four fields surveyed in this work. Other sightlines from the literature are discussed in Section 5.3.

We consider the three main types of models described in the introduction: fluctuating UVB, fluctuating temperature, and ultra-late reionization. Of these three types of models, we consider six variations. Two are galaxy-driven UVB models, one from Davies et al. (2018a) and another, which also includes temperature fluctuations as would be expected at the end of reionization, from Nasir & D'Aloisio (2020). A third UVB model, from Chardin et al. (2015, 2017), is quasar-driven. The fourth is a fluctuating temperature model from D'Aloisio et al. (2015). Lastly, we consider two variations on an ultra-late reionization scenario from Nasir & D'Aloisio (2020). These models incorporate fluctuations in temperature and UVB as expected at the end of reionization, but allow the IGM to be $\sim 10\%$ neutral at $z = 5.5$. Of these two models, one uses a short mean free path (8 h^{-1} Mpc at z=6) and the other a long mean free path (23 h^{-1} Mpc at $z = 6$). For comparison, Becker et al. (2021) measure a mean free path of 3.57 h^{-1} Mpc at $z = 6$.

The predictions for surface density of LAEs as a function of radius are constructed from sightlines that have $\tau^{50}_{\rm eff} = 2.5 \pm 0.25$ (transmissive predictions) or $\tau^{50}_{\rm eff} \geq 7.0$ (opaque predictions). We note that the J1250 sightline has $\tau^{50}_{\rm eff} = 5.033 \pm 0.215$, which is somewhat lower than the simulated opaque sightlines used here; however, Davies et al. (2018a) find that model predictions for $\tau^{50}_{\rm eff} \geq 5.0$ are very similar (see also Figure 10). For each model, simulated LAE populations around these sightlines are constructed using the following basic procedure: galaxies are assigned to dark matter halos, using the measured UV luminosity of Bouwens et al. (2015) for abundance matching, and their spectra are modeled as a power-law continuum with a Lyα emission line with equivalent width set by the models of Dijkstra & Wyithe (2012). We refer the reader to Nasir & D'Aloisio (2020) and Davies et al. (2018a) for further details.

To ensure that the comparison between the modelled LAE populations and our models is as close as possible, we match the surface density of the model population to that of the observed population. First, we remove simulated LAEs from the sample in a radially- and magnitude-weighted manner using the observed completeness correction to create an incomplete catalog of simulated LAEs, comparable to the raw, uncorrected observations. The completeness correction is scaled by a factor of ~ 0.6, so that the mean surface density of the incomplete simulated LAEs matches the uncorrected median surface density of real LAEs in our four fields. We then apply the completeness correction without the scaling factor, as done with the real LAEs, to produce a completeness-corrected simulated LAE population. From this completeness-corrected sample, we construct expected surface density profiles for highly opaque and transmissive lines of sight, which we compare to our

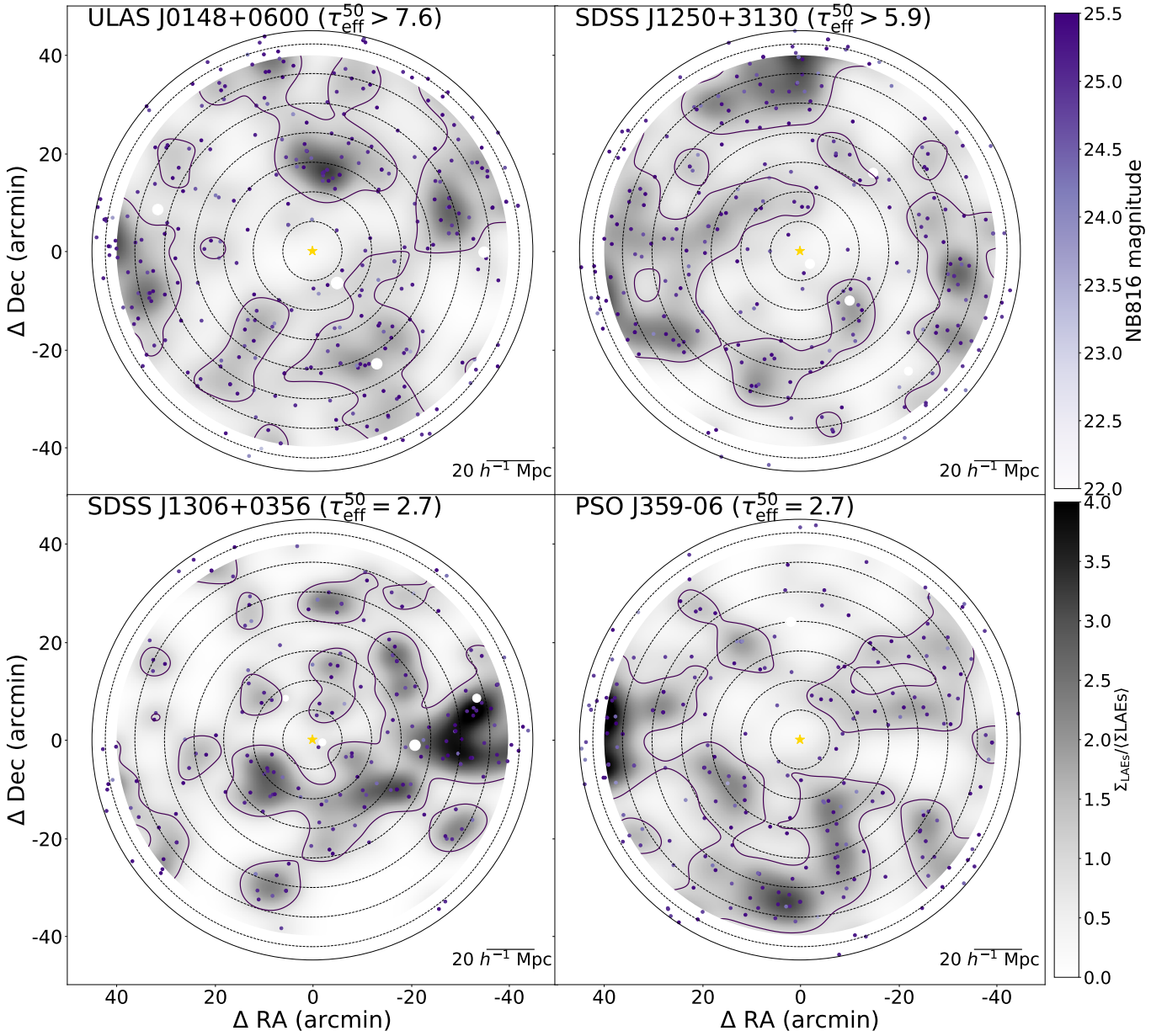

Figure 6. Distribution of LAE candidates in all four fields: J0148 (top left), J1250 (top right), J1306 (bottom left), and J359 (bottom right). The LAE candidates are assigned a color that indicates their NB816 magnitude. The grayscale shading in the background indicates the surface density of LAE candidates, which we calculate by kernel density estimation and normalized by the mean surface density of each field, measured over $15' \leq \Delta\theta \leq 40'$. This surface density is corrected for spatial variations in completeness as described in Section 3.3. The field is centered on the quasar position, which is marked with a gold star, and the concentric dotted rings indicate 10 h^{-1} Mpc intervals from the quasar position. The solid ring marks the edge of the field, $45'$ from the quasar position. Portions masked out of the field in white are obscured by foreground stars.

measurements.

Figure 8 shows the measured surface density in the J0148 (filled circle) and J1250 (open triangle) fields as a function of radius alongside model predictions for opaque sightlines. Similarly, Figure 9 shows the comparison between the measured surface density in the J1306 (filled circle) and J359 (open triangle) fields as a function of radius and model predictions for transmissive sightlines. In both sets of figures, the top row shows, from left to right, predictions from the galaxy UVB model (Davies et al. 2018a), quasar UVB model (Chardin et al. 2015, 2017), and temperature model (D'Aloisio et al. 2015). The bottom row shows, from left to right, predictions from Nasir & D'Aloisio (2020) for the galaxy UVB model, the ultra-late reionization model with a long mean free path, and the ultra-late reionization model with a short mean free path. In each panel, the mean model prediction is shown with a solid line, and the shaded regions indicate the 68% and 98% ranges. All predictions and measurements measurements are normalized over the mean surface density in each field, measured over $15' \leq \theta \leq 40'$. In this figure, and in others following that compare our observations to models, we have omitted vertical error bars. The ranges we give in Table 3 are based on Poisson statistics, and including them here would imply that the field-to-field variations are based primarily on shot noise rather

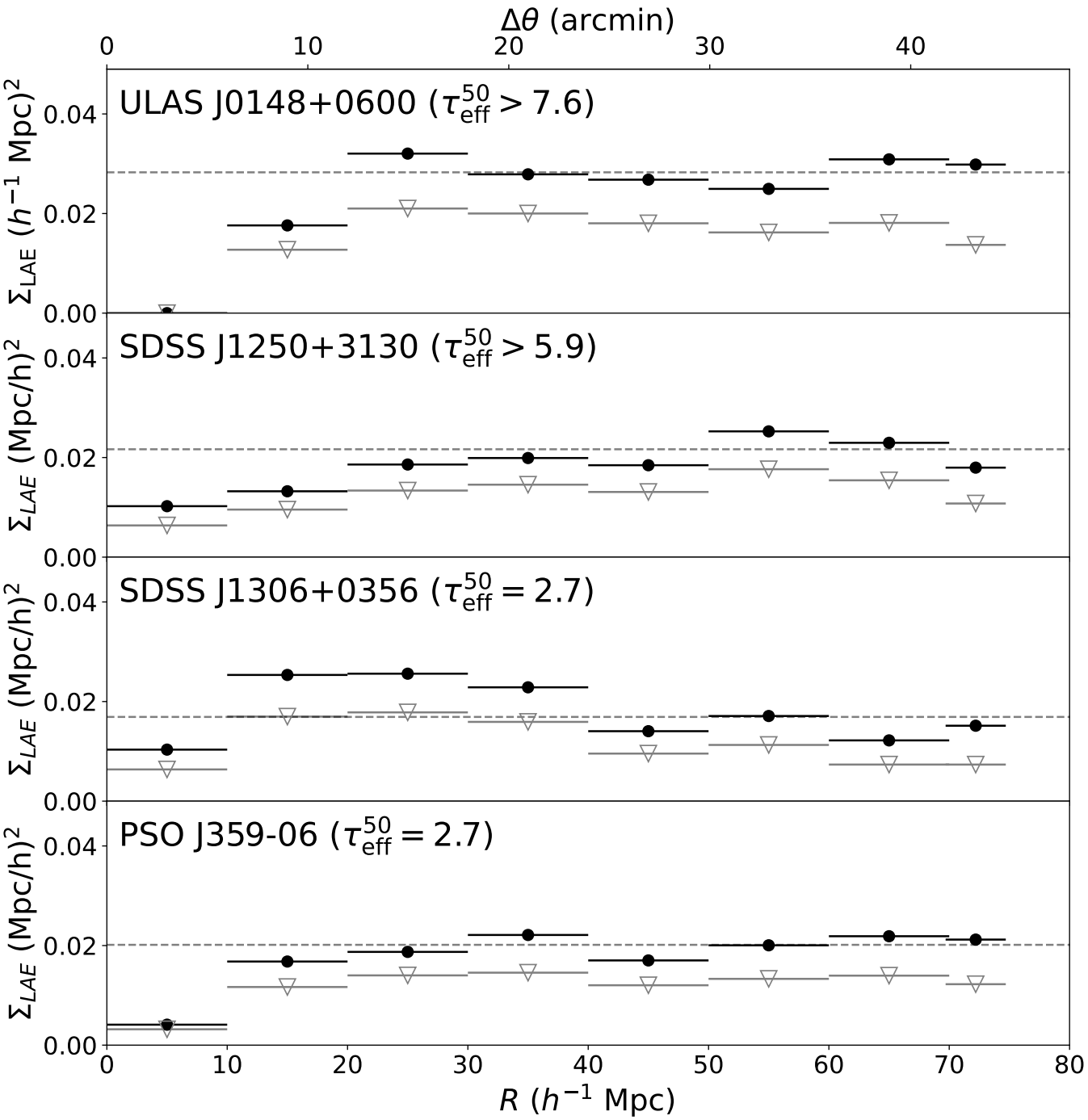

Figure 7. Surface density of LAE candidates in all four fields (from top to bottom: J0148, J1250, J1306, J359) as a function of their distance from the quasar position, measured in 10 h^{-1} Mpc annular bins. The unfilled gray triangles indicate raw surface density measurements, and the filled black circles indicate completeness-corrected measurements. The dotted line represents the mean completeness-corrected surface density in the field measured over $15' \leq \Delta\theta \leq 40'$. The horizontal error bars indicate the width of the annulus.

than cosmic variance. The purpose of these figures is to consider whether our observations could be individual realizations of these models based on the range of density values expected for individual fields in each model. The most relevant variance for this comparison is therefore the model variance.

We find that all four sightlines are underdense within 10 h^{-1} Mpc of the quasar sightline, compared to the mean surface density of the exterior of the field. The highly opaque sightlines strongly disfavor the temperature model but are consistent with predictions from the UVB and late reionization models, as found in Becker et al. (2018) and Christenson et al. (2021). There is some tension, however, between the transmissive sightlines and these models. The J359 sightline falls below the lower 98% threshold at $R \leq 10h^{-1}$ Mpc for all four of the galaxy UVB and late reionization models, and the J1306 model falls below the lower 68% threshold in the same

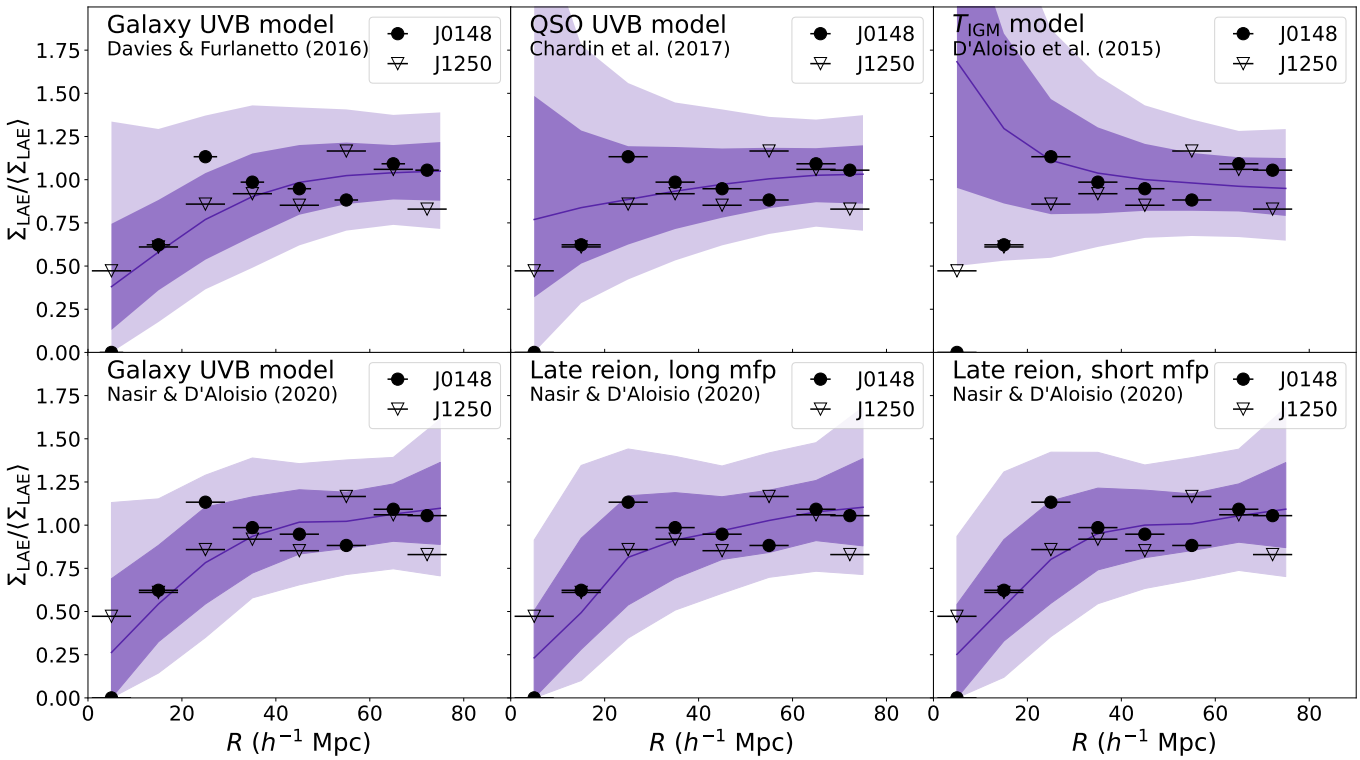

Figure 8. Surface density profiles for highly opaque lines of sight. Each panel compares the observed radial distribution of LAE candidates in the J0148 (filled circle) and J1250 (open triangle) fields to model predictions, where the model lines of sight have $\tau_{\rm eff}^{50} \geq 7.0$. The top row shows predictions from the galaxy UVB model based on Davies & Furlanetto (2016) (top left), the QSO UVB model based on Chardin et al. (2015, 2017) (top center), and the fluctuating temperature model from D'Aloisio et al. (2015) (top right). The bottom row shows predictions from Nasir & D'Aloisio (2020), including their galaxy UVB (early reionization) model (bottom left), late reionization model with a long mean free path (bottom center), and late reionization model with a short mean free path (bottom right). The solid lines show the median predictions for each model. The dark- and light-shaded regions show 68% and 98% ranges respectively. As in Figure 7, the horizontal error bars on the data points indicate the width of the bins. All surface densities are given normalized by the mean surface density in the field, measured over $15' \leq \theta \leq 40'$.

ranges. This suggests that these models are unlikely to produce transmissive sightlines that are as underdense as the two we have observed. Taking all four sightlines into account, none of the models we consider here are obviously consistent with all of the data.

5.2. *Environments of extreme-opacity sightlines*

A main focus of this paper is interpreting the four sightlines together, to consider what we can infer about the environments in which extreme opacity sightlines arise. The two highly opaque sightlines clearly show underdense regions within 20 h^{-1} Mpc of the quasar sightline. Similarly, the J359 sightline sits in an underdense region that is longer, but narrower, running in roughly the east-west direction. These underdense regions have a large lateral extent, spanning tens of comoving megaparsecs. The opaque troughs extend over 160 and 80 h^{-1} Mpc (J0148 and J1250 respectively), and the J359 sightline is transmissive over a 50 h^{-1} Mpc segment of the Lyα forest. We consider a region transmissive based on the absence of dark gaps ($\geq 30h^{-1}$ Mpc in length, as defined by Zhu et al. 2021) - or, more simply, that it is populated by transmission spikes that are measurable in extent relative to the continuum level. The lateral extent of these underdensities suggests that, were they to also extend over the full lengths of the corresponding Lyα forest features, these extreme sightlines could arise from very large structures.

The J1306 sightline arises from a region that is underdense, but adjacent to overdense regions. Approximately 45% of the area within 20 h^{-1} Mpc of the quasar sightline is estimated to be overdense (Figure 6), compared to 7% (J0148), 14% (J1250), and 19% (J359) for the other fields. The galaxy overdensity ~ 30 h^{-1} Mpc to the west of the J1306 sightline is particularly extensive. Given that the J1306 sightline is highly transmissive, the proximity of these potential sources of ionizing photons raises the question of whether these nearby overdense regions play a significant role in ionizing the IGM in the vicinity of the quasar sightline. The recent measurement of the mean free path at $z = 6.0$ by Becker et al. (2021) makes it possible to estimate what the mean free path should be at $z = 5.7$. Becker et al. (2021) measure $\lambda_{\rm mfp} = 9.09^{+1.62}_{-1.28}$ proper Mpc at $z = 5.1$, and $\lambda_{\rm mfp} = 0.75^{+0.65}_{-0.45}$ proper Mpc at $z = 6.0$. Linearly interpolating between these two measurements, we find that the mean free path at $z = 5.7$ should be approximately $\lambda_{\rm mfp} = 3.5$ proper Mpc, which corresponds to 16.4 h^{-1} comoving Mpc. Referring to Figure 6, if $\lambda_{mfp} = 16.4$ h^{-1} Mpc, then parts of the overdense regions in the J1306 field lie within a mean free path of the sightline. While this is a rough approximation, given that the mean free path will vary locally, it is at least plausible that these nearby overdense regions could contribute to the ionization state of the IGM in the vicinity of the quasar sightline. We also find that,

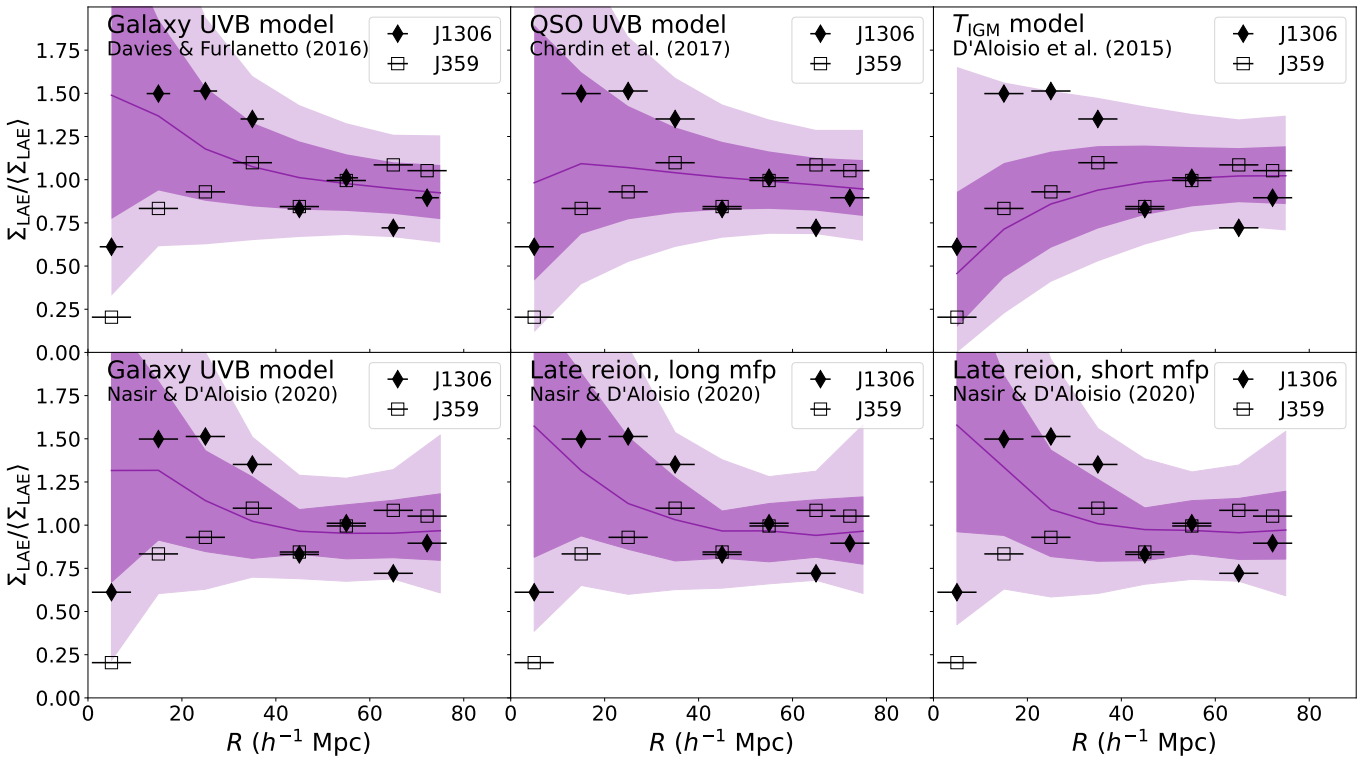

Figure 9. Surface density profiles for transmissive lines of sight. Each panel compares the observed radial distribution of LAE candidates in the J1306 (filled circle) and J359 (open triangle) fields to model predictions. The models are the same as in Figure 8, but for model lines of sight with $\tau_{\rm eff}^{50} = 2.5 \pm 0.25$. Lines, shading, and error bars are as in Figure 8. All surface densities are given normalized by the mean surface density in the field, measured over $15' \leq \theta \leq 40'$.

for the simulated sightlines of Nasir & D'Aloisio (2020), highly transmissive, low-density sightlines are more likely to show an overdensity in adjacent radial bins in their surface density profile (similar to the J1306 field in Figure 7) than their higher-opacity counterparts. For example, of the sightlines in the late reionization, short mean free path model, 55% of the sightlines with $\tau_{\rm eff}^{50} \leq 3.0$ and normalized surface density ≤ 0.5 within $R \leq 10\ h^{-1}$ Mpc also had a normalized surface density of ≥ 1.25 in either the $10-20$ or $20-30\ h^{-1}$ Mpc bin, compared to 11% of sightlines with $\tau_{\rm eff}^{50} \geq 5.0$. This trend holds for all three models of Nasir & D'Aloisio (2020), which suggests that adjacent overdensities may play a role in the high transmission of these sightlines. There is evidence from the literature that suggests LAEs may enhance the local photoionizating background. Meyer et al. (2019, 2020) report an excess of Lyα transmission spikes within $10-60$ cMpc from LAEs; this relationship between Lyα flux and galaxy distance is additionally well-matched by the THESAN models (Garaldi et al. 2022). Similarly, Kakiichi et al. (2018) find that IGM Lyα transmission is preferentially higher in the vicinity of luminous Lyman break galaxies, many of which also show Lyα lines, and (Kashino et al. 2023) find that IGM Lyα transmission peaks 5 Mpc from [OIII] emitting galaxies at $5.7 < z < 6.14$. Given this observed link between galaxies and elevated Lyα transmission, one possible interpretation of our observations of transmissive sightlines is that they can arise in less dense regions that are close enough to an overdensity to have an elevated ionizing background that contributes to its highly transmissive state. This interpretation is qualitatively consistent with both the galaxy UVB and ultra-late reionization scenarios.

5.3. *Opacity-density relation*

Now that a number of extreme opacity QSO fields have been surveyed for LAEs, we can begin to characterize the relationship between Lyα opacity and galaxy density at $z \sim 5.7$. Figure 10 shows the measured surface density in the inner $10\ h^{-1}$ Mpc of all four fields as a function of the Lyα effective opacity. Also shown are the predictions for the relationship between surface density of LAEs and Lyα opacity in each of the models. These measurements are normalized by the mean surface density in their respective fields.

The surface density measurements for transmissive sightlines put some pressure on fluctuating UVB and late reionization models, as the J359 measurement falls outside 98% range for some of the model predictions. Further, we note that all four surface density measurements lie near or below the median predictions for all models. This outcome is unlikely to occur randomly; there is only a 6.25% chance that four randomly drawn sightlines would lie below the median. The probability of reproducing our densities is as low as $< 2\%$, moreover, given that some of the measurements lie below the 68% and 98% thresholds for the different models. This emphasizes the possibility that none of the models accurately capture the relationship between opacity and density across the full $\tau_{\rm eff}$ range.

In addition to the four fields presented in this work, three additional fields have been surveyed by Ishimoto

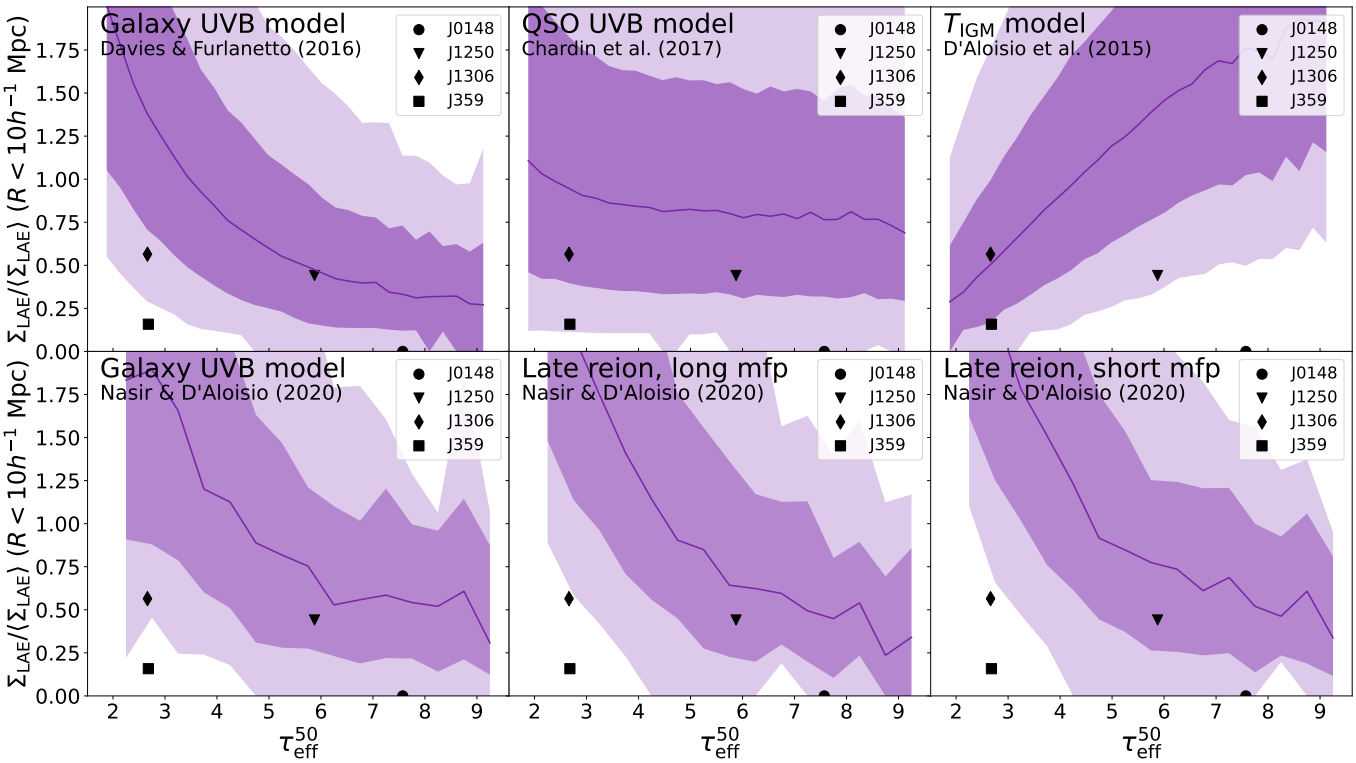

Figure 10. Comparison of the measured surface density of LAE candidates within 10 h^{-1} Mpc of the quasar sightline to model predictions for the relationship between opacity and LAE density. The models are the same as those in Figures 8 and 9 and predictions are made using the full set of model sightlines spanning all opacity values. All surface densities are given normalized by the mean surface density measured over $15' \leq \theta \leq 40'$in each individual field.

et al. (2022). Their fields have $\tau_{\rm eff}$ values measured over 50 h^{-1} Mpc of 4.17±0.25, 2.85±0.04, and 2.91±0.03, where these values are re-measured here from spectra reduced with a custom pipeline optimized for high-redshift QSOs (see Appendix B). Of these fields, the two with transmissive $\tau_{\rm eff}^{50}$ values are overdense, and the one with moderate $\tau_{\rm eff}^{50}$ is underdense in the vicinity of the quasar sightline. The $\tau_{\rm eff}$ values for all seven fields are summarized in Table 1.

In Figure 11, we show the surface density in the inner 10 h^{-1} Mpc of all seven quasar sightlines as a function of their $\tau_{\rm eff}^{28}$ (left panel) and $\tau_{\rm eff}^{50}$ (right panel). We use the bright limit from Ishimoto et al. (2022) of NB816$\leq$ 25.2 for all fields. The surface density measurement in each field is normalized by the mean surface density in that field, measured over $15 \leq \theta \leq 40$ arcmin, as is done elsewhere in this work.

In principle, the seven combined fields from this work and Ishimoto et al. (2022) present an opportunity to evaluate the opacity-density relation with greater sampling of the $\tau_{\rm eff}$ distribution. At face value, low-$\tau_{\rm eff}$ lines of sight with high densities would support the fluctuating UVB and late reionization models. In practice, however, directly comparing these fields presents challenges. Field-to-field variations in depth and seeing and differences in methods for photometry, LAE selection, and completeness corrections all complicate the comparison (see (Ishimoto et al. 2022) for an overview of their methodology). Further, the two sets of sightlines presented in this work and in Ishimoto et al. (2022) were selected in different manners. Our two highly opaque sightlines, J0148 and J1250, were selected based on the presence of long Lyα troughs of 110 h^{-1} and 81 h^{-1} Mpc respectively. The J1306 and J359 sightlines were selected based on their $\tau_{\rm eff}^{50}$ values, although the J1306 sightline was known to be transmissive over a longer segment of the Lyα forest (eg Becker et al. 2015). In contrast, Ishimoto et al. (2022) selected their fields based on Lyα forest opacities over the wavelength range of the NB816 filter, which corresponds to ∼28 h^{-1} Mpc. For a comparison of the $\tau_{\rm eff}$ measurements over 28 and 50 h^{-1} Mpc windows, see Table 1. Our sightlines have similar $\tau_{\rm eff}$ values over these windows. Two of the three sightlines from Ishimoto et al. (2022), however, show significant differences in their 28 or 50 h^{-1} Mpc opacities. In these cases, the forest is highly opaque over the 28 h^{-1} Mpc window but shows strong transmission just outside it, giving a lower 50 h^{-1} Mpc opacity. Because the sightlines from Ishimoto et al. (2022) were selected to be opaque over 28 h^{-1} Mpc, they may not be representative of all sightlines with low $\tau_{\rm eff}^{50}$. Figure 11 illustrates the strong impact that the $\tau_{\rm eff}$ measurement window has on the results.

To understand the biases associated with selecting sightlines over the $NB816$ window, we investigated similar sightlines in the fluctuating UVB and late reionization models from Nasir & D'Aloisio (2020). We selected sightlines with $\tau_{\rm eff}^{28} \geq 4.0$ and $\tau_{\rm eff}^{50} \leq 3.0$, similar to the sightlines from Ishimoto et al. (2022). Of the 4000 simulated sightlines for each model, there are 10−15 sightlines that meet these criteria. Similar to the real sightlines, the simulated ones uniformly show a strongly absorbed dark gap over the $NB816$ filter range, and strong transmission

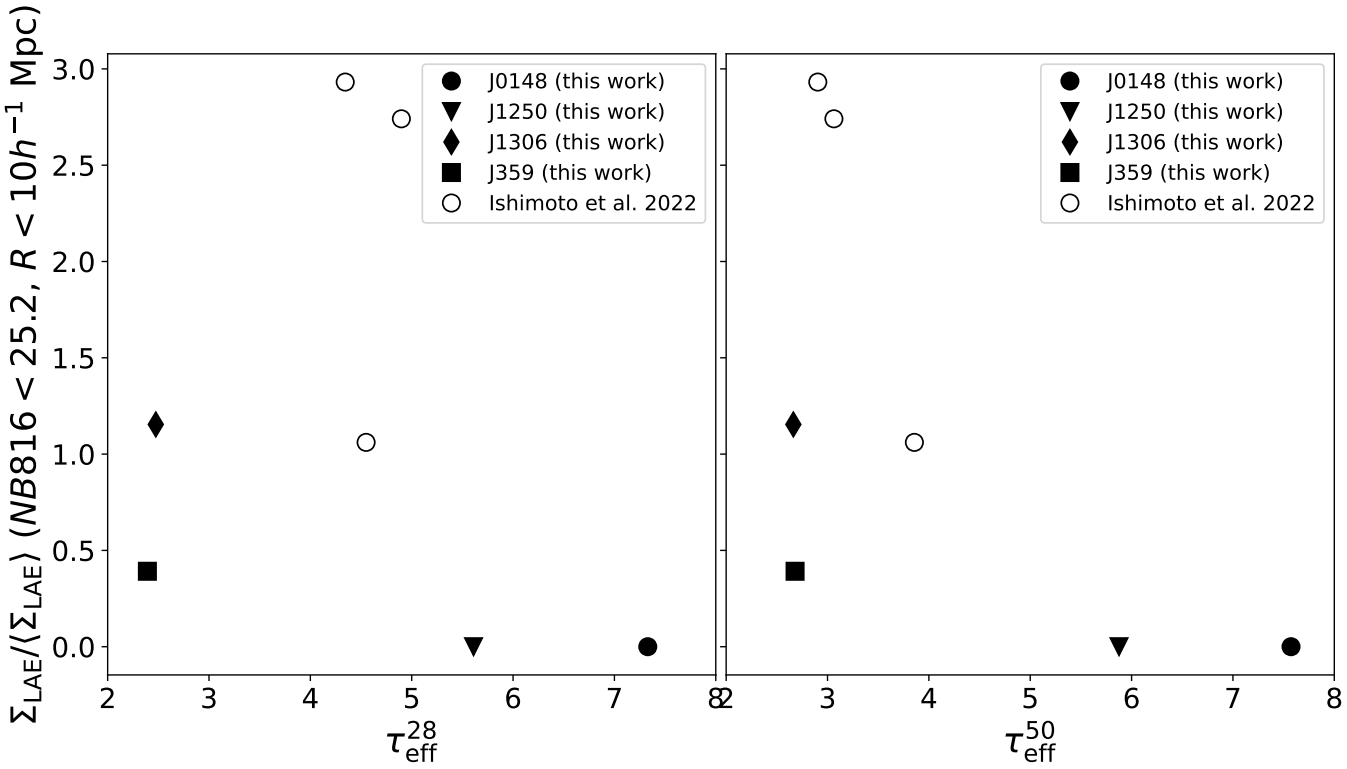

Figure 11. Measured surface density of LAE candidates within 10 h^{-1} Mpc of the quasar sightline as a function of $\tau_{\rm eff}^{28}$ (left) and $\tau_{\rm eff}^{50}$ (right). We include both $\tau_{\rm eff}$ windows here for comparison; for a discussion of the selection biases associated with each, see Section 5.3. Included are all seven fields surveyed to date, presented in this work and Ishimoto et al. (2022). For all seven fields, we match observational considerations as closely as possible, including the limiting magnitude, window of the $\tau_{\rm eff}$ measurement, and normalization. LAEs in all fields are selected down to the bright limit from Ishimoto et al. (2022) of NB816$\leq$ 25.2. Surface densities are given normalized by the mean surface density measured over $15' \leq \theta \leq 40'$in each field.

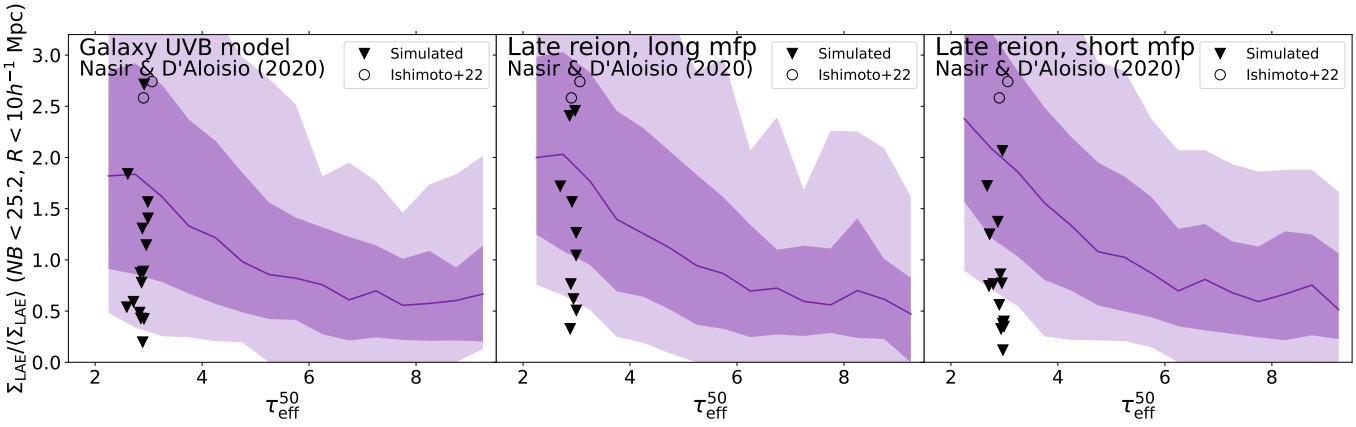

Figure 12. Measured surface density of LAE candidates within 10 h^{-1} Mpc of the quasar sightline as a function of $\tau_{\rm eff}^{50}$, for sightlines from Ishimoto et al. (2022) and simulated sightlines from the models of Nasir & D'Aloisio (2020). The simulated sightlines were selected to have $\tau_{\rm eff}^{28} \geq 4.0$ and $\tau_{\rm eff}^{50} \leq 3.0$, similar to the two overdense sightlines of Ishimoto et al. (2022). The model predictions are made using $\tau_{\rm eff}^{50}$ values, and all surface densities are given normalized by the mean surface density measured over $15' \leq \theta \leq 40'$in each individual field. This figure illustrates that although these two lines of sight fall in the upper density range for their $\tau_{\rm eff}^{50}$ values, they are not consistent with simulated lines of sight from these models that were selected in the same way.

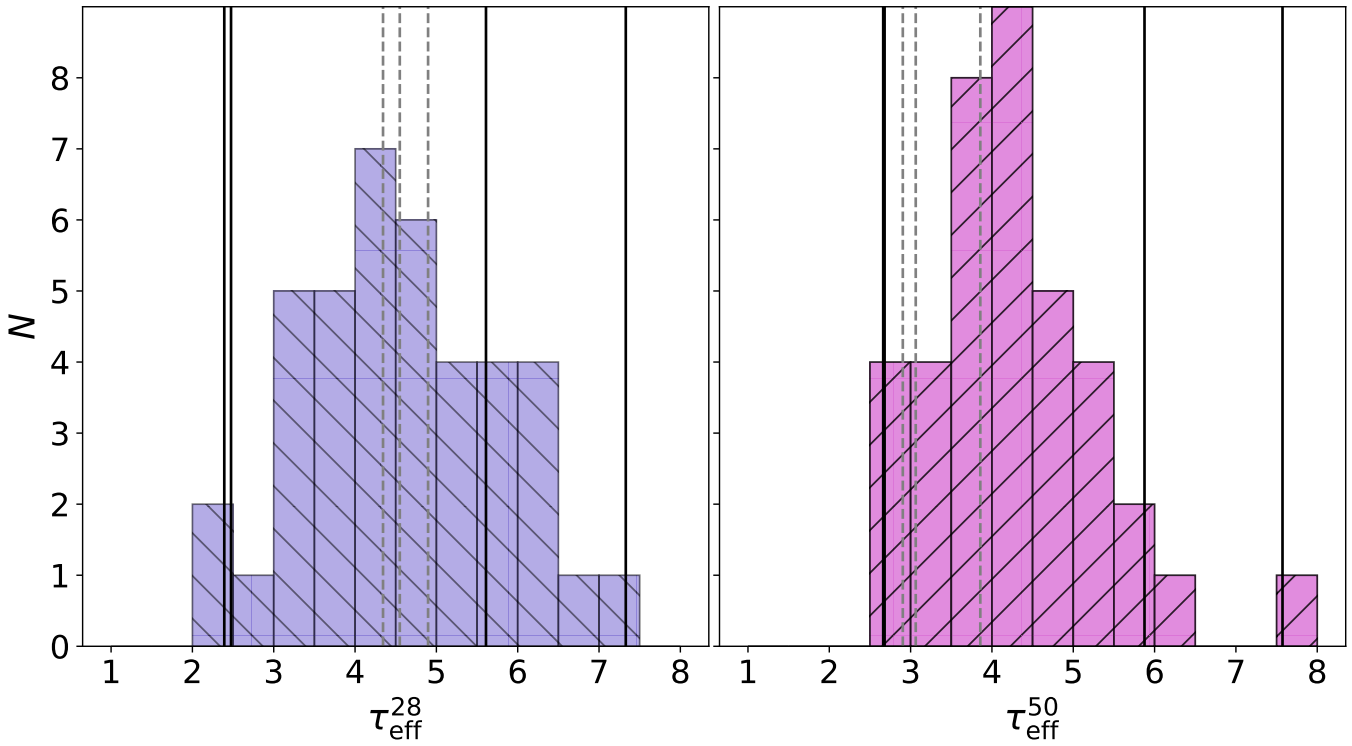

Figure 13. Distribution of $\tau_{\rm eff}$ measurements for the quasar sample from Zhu et al. (2021), measured both over 28 h^{-1} Mpc (left) and 50 h^{-1} Mpc (right). We show where the sightlines from this work and Ishimoto et al. (2022) fall in the distribution with solid black and dashed gray vertical lines, respectively. The sightlines from this work all fall in the wings of the global distribution, whereas the sightlines from Ishimoto et al. (2022) are more moderate.

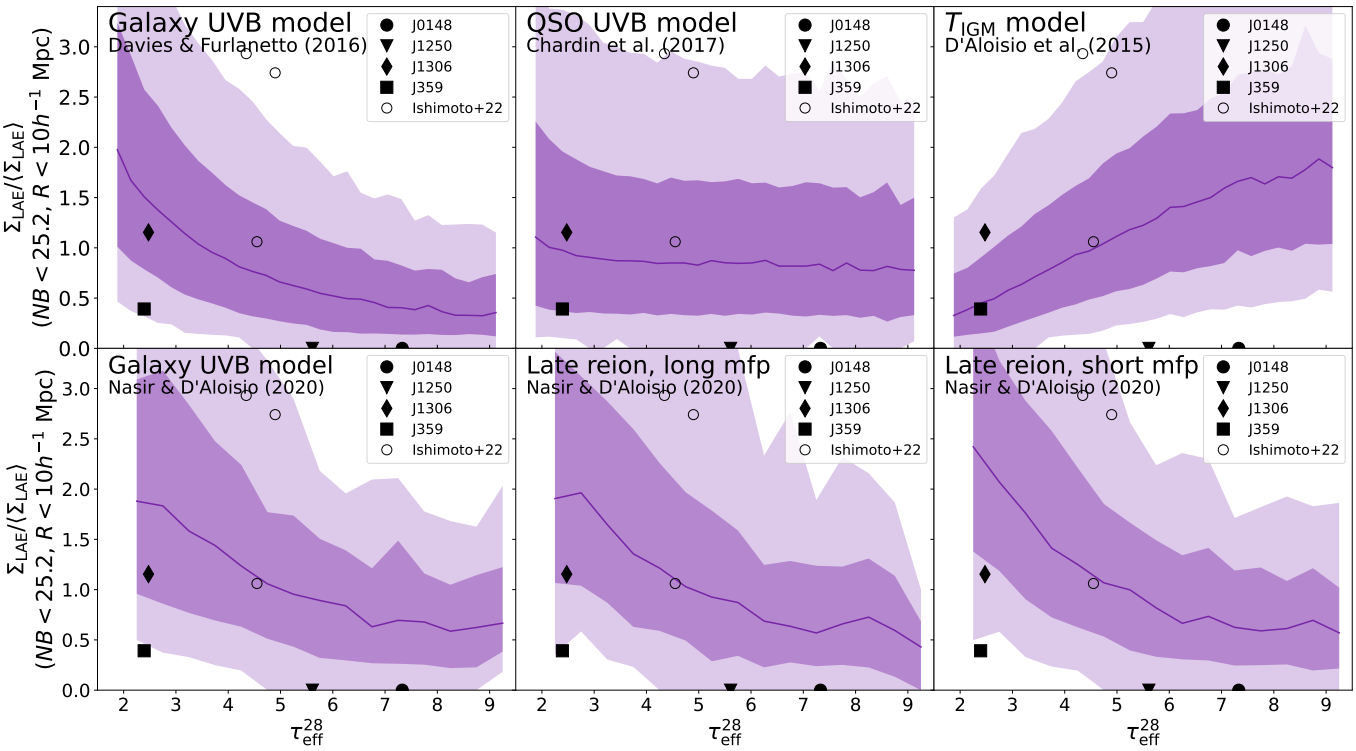

Figure 14. Comparison of the measured surface density of LAE candidates within 10 h^{-1} Mpc of the quasar sightline to model predictions for the relationship between opacity and LAE density. The models are the same as those used in Figures 8,9, and 10. Both observations and model predictions use opacity measurements made over 28 h^{-1} Mpc and the $NB816 \leq 25.2$ magnitude limit of Ishimoto et al. (2022). All surface densities are given normalized by the mean surface density measured over $15' \leq \theta \leq 40'$in each individual field.

spikes over the remainder of the 50 h^{-1} Mpc window. The densities of these sightlines sample the full range of density scatter shown in model predictions for density as a function of $\tau_{\rm eff}^{28}$. However, they are not representative of the density distribution for sightlines that are transmissive over 50 h^{-1} Mpc. Figure 12 shows the surface density of these simulated sightlines and the sightlines observed by Ishimoto et al. (2022) compared to model predictions made over 50 h^{-1} Mpc. Simulated sightlines that are selected to be opaque over 28 h^{-1} Mpc are biased towards being underdense for their 50 h^{-1} Mpc opacities. The two Ishimoto et al. (2022) sightlines with these opacity characteristics are denser than any of the simulated sightlines that were selected in the same manner. These sightlines are therefore also not obviously consistent with either the UVB or late reionization models.

We suggest that the $\tau_{\rm eff}^{28}$ window may be least impacted by selection effects because it reflects the selection criteria of Ishimoto et al. (2022) and because the $\tau_{\rm eff}$ measurements for the sightlines presented in this work are fairly consistent over both windows. At the limit of $NB816 < 25.5$ used in Figure11, highly opaque sightlines (on scales of 28 h^{-1} Mpc) are correlated with galaxy underdensities, while the transmissive sightlines are mildly over- or underdense. Sightlines with moderate opacity, meanwhile, show a large scatter in observed density. Overall, three of the seven sightlines surveyed are underdense within 10 h^{-1} Mpc of the quasar sightline and two are of average density. Although the overall sample tends towards lower densities, we note that most of these sightlines are selected to be atypical in terms of their $\tau_{\rm eff}$ values, and we do not expect them to average to unity as we would a larger, more representative sample. Figure 13 shows the distribution of $\tau_{\rm eff}$ values for the quasar sample of Zhu et al. (2021) measured over both 28 (left) and 50 (right) h^{-1} Mpc windows. The opacity values for the sightlines discussed in this work are marked with vertical lines. The four sightlines presented in this work, which are mostly underdense, fall at the extreme ends of the distribution. The sightlines from Ishimoto et al. (2022), which show a range of densities, fall in the center of the global distribution and are likely to be more representative of the majority of quasar sightlines at this redshift.

Figure 14 shows the surface density within 10 h^{-1} Mpc of the quasar sightline as a function of $\tau_{\rm eff}^{28}$ for all sightlines from this work and Ishimoto et al. (2022), compared to predictions from the models of Nasir & D'Aloisio (2020). Both the data and models use $\tau_{\rm eff}^{28}$ opacity measurements and the $NB816 \leq 25.2$ magnitude limit of Ishimoto et al. (2022). We use $\tau_{\rm eff}^{28}$ values for this model comparison because they may be less impacted by selection effects than $\tau_{\rm eff}^{50}$ values, as discussed above.

Altogether, these observations are not clearly consistent with any of the models considered here. The association of highly opaque sightlines and galaxy underdensities is explained well by fluctuating UVB and late reionization models, but these models do not obviously work well for the transmissive sightlines. On the other hand, the temperature model is in good agreement with the transmissive sightlines.

We can speculate on what may be happening at the low-opacity end. In a post-reionization IGM with a more homogeneous UVB, we expect that opacity will positively correlate with density. This correlation may even be enhanced by temperature fluctuations for some period following reionization, as in the fluctuating temperature model. A homogeneous UVB is not expected at $z = 5.7$; indeed, there is strong observational evidence for UVB fluctuations persisting as late as $z \sim 5.3$ (Becker et al. 2015; Bosman et al. 2018; Eilers et al. 2018; Yang et al. 2020; Bosman et al. 2021; Zhu et al. 2021). If the UVB is not as highly suppressed in underdense regions as the models considered here suggest, however, then these regions may quickly transition from being highly opaque to being transmissive once they are fully reionized, an evolution first suggested by Keating et al. (2020b).

A caveat of this work is the assumption that LAEs are a good tracer of the underlying density field, an assumption that is complicated near the end of reionization by how susceptible Lyα photons are to attenuation by neutral gas. Davies et al. (2018a) found that LAE surveys were ∼90% likely to distinguish between fluctuating UVB and temperature models. However, there is some observational evidence, albeit at lower redshift, that LAEs either avoid some high-density peaks (Francis & Bland-Hawthorn 2004; Kashikawa et al. 2007; Huang et al. 2022), or tend to prefer lower-density regions (Cooke et al. 2013), possibly because higher-density regions have a stronger UVB that suppresses star formation (Kashikawa et al. 2007; Bruns et al. 2012). Kashino et al. (2020) surveyed Lyman break galaxies (LBGs) in the J0148 field and found an underdensity in the vicinity of the quasar sightline, which indicates that the J0148 underdensity is not the result of Lyα suppression by neutral gas. However, it is unclear whether LBGs and LAEs in this field trace the same large scale structures, in part due to the broader redshift range spanned by the LBG selection ($\Delta z \sim 0.4$). It is also unclear whether a survey of LBGs in a field surrounding a transmissive sightline would similarly show the same density profile as the LAE population. A promising avenue for future work is therefore to consider other types of galaxy surveys to corroborate the results of the LAE selections. In addition to LBGs, sub-mm sureys, which probe massive, obscured galaxies, may be a useful probe of the density at these redshifts; Li et al. (2023) recently surveyed sub-mm galaxies in the J0148 field and reported an overdensity, although without redshifts it is unclear whether they are in proximity to the Lyα trough. It is also now possible to select galaxies at these redshifts based on their [OIII]$\lambda\lambda$4960,5008 emission with JWST/NIRCam, as done by the EIGER team (Kashino et al. 2023).

6. SUMMARY

We present an initial characterization of the relationship between IGM Lyα opacity and galaxy density at $z = 5.7$ by surveying Lyman-α emitting galaxies in the fields surrounding quasar sightlines with extreme values of Lyα opacity. The relationship between IGM opacity and galaxy density on large ($\gtrsim 10$ h^{-1} Mpc) transverse scales serves as a test of reionization models that predict the observed scatter in Lyα opacity. Surveying sightlines over a wide range of Lyα opacity, particularly extreme values, is necessary to characterize this relationship. We present two new surveys of LAEs towards the $z = 6.02$ quasar SDSS J1306+0356 and the $z = 6.17$

quasar PSO J359-06, whose sightlines show very low effective Lyα opacity over 50 h^{-1} Mpc along the line of sight ($\tau_{\rm eff}^{50} = 2.6$ and $\tau_{\rm eff}^{50} = 2.7$ for the J1306 and J359 fields respectively). We also re-select LAEs in the fields surrounding two highly opaque sightlines, towards ULAS J0148+0600 and SDSS J1250+3130, using the aperture photometry adopted for this work.

We report an underdensity of LAEs within 10 h^{-1} Mpc of both transmissive quasar sightlines. The results towards highly opaque sightlines are unchanged from previous works (Becker et al. 2018; Christenson et al. 2021); we find strong underdensities in the vicinity of both quasar sightlines. We note that the underdensities associated with Lyα troughs span greater lateral extent than those associated with transmissive sightlines ($\gtrsim$ 20 h^{-1} Mpc; see Section 5.2). We compare the measured surface density as a function of radius to predictions made by three broad types of models in Figure 9: fluctuating UVB models (Davies et al. 2018a; Nasir & D'Aloisio 2020; Chardin et al. 2015, 2017), fluctuating temperature models (D'Aloisio et al. 2015), and ultra-late reionization models (Nasir & D'Aloisio 2020, see also Kulkarni et al. 2019; Keating et al. 2020a. The correlation between highly opaque sightlines and galaxy underdensities strongly disfavors the temperature model, and the fluctuating UVB and late reionization models are unlikely to produce transmissive sightlines as underdense as those we observe. None of the models, on their own, cleanly predict our observations of all four sightlines.

Our measurements allow us to begin characterizing the observed LAE surface density as a function of Lyα effective opacity (see Figure 10). The highly transmissive sightlines are sufficiently underdense within 10 h^{-1} Mpc of the quasar sightline to be challenging for galaxy-driven UVB and late reionization models, which favor overdense regions associated with transmissive sightlines. Further, all of our observations fall below the median model predictions for the opacity-density relation, which hints that the models may not fully capture the physical conditions leading to sightlines with extreme opacity.

A total of seven fields surrounding quasar sightlines have now been surveyed in this manner. We show the LAE surface density as a function of Lyα effective opacity of our four fields together with three from Ishimoto et al. (2022) (Figure 11). While the sightlines with extreme opacity are correlated to galaxy underdensities within 10 h^{-1} Mpc of the quasar sightline, the sightlines of moderate opacity range from median density to significantly overdense. The association of highly opaque sightlines with galaxy underdensities is well-predicted by UVB and late reionization models. The association of highly transmissive sightlines with galaxy underdensities, however, is in possible tension with these models. One possible interpretation of these observations is that as reionization ends, the UVB transitions to a more homogeneous state more quickly than in the models considered here, causing the hot, recently reionized voids to rapidly become highly transmissive. This evolution in the transmission of the voids was first suggested by Keating et al. (2020b).

Further galaxy surveys, particularly towards transmissive sightlines, are needed for a more robust characterization of the relationship between opacity and density. If these further observations confirm the correlation between transmissive sightlines and galaxy underdensities, it would indicate that current reionization models do not adequately capture the ionizing sources and/or the sinks near the end of reionization.

H.C. is supported by the National Science Foundation Graduate Research Fellowship Program under Grant No. DGE-1326120. H.C., G.B. and Y.Z. are supported by the National Science Foundation through grant AST-1615814 and AST-1751404. S.R.F. is supported by the National Science Foundation through awards AST-1812458 and AST-2205900 and by NASA through award 80NSSC22K0818.

This research is based in part on data collected at Subaru Telescope, which is operated by the National Astronomical Observatory of Japan. We are honored and grateful for the opportunity of observing the Universe from Maunakea, which has cultural, historical and natural significance in Hawaii. The Hyper Suprime-Cam (HSC) collaboration includes the astronomical communities of Japan and Taiwan, and Princeton University. The HSC instrumentation and software were developed by the National Astronomical Observatory of Japan (NAOJ), the Kavli Institute for the Physics and Mathematics of the Universe (Kavli IPMU), the University of Tokyo, the High Energy Accelerator Research Organization (KEK), the Academia Sinica Institute for Astronomy and Astrophysics in Taiwan (ASIAA), and Princeton University. Funding was contributed by the FIRST program from Japanese Cabinet Office, the Ministry of Education, Culture, Sports, Science and Technology (MEXT), the Japan Society for the Promotion of Science (JSPS), Japan Science and Technology Agency (JST), the Toray Science Foundation, NAOJ, Kavli IPMU, KEK, ASIAA, and Princeton University.

This research is based in part on observations collected at the European Organisation for Astronomical Research in the Southern Hemisphere under ESO programmes 084.A-0390, and 1103.A-0817.

The Pan-STARRS1 Surveys (PS1) have been made possible through contributions of the Institute for Astronomy, the University of Hawaii, the Pan-STARRS Project Office, the Max-Planck Society and its participating institutes, the Max Planck Institute for Astronomy, Heidelberg and the Max Planck Institute for Extraterrestrial Physics, Garching, The Johns Hopkins University, Durham University, the University of Edinburgh, Queens University Belfast, the Harvard-Smithsonian Center for Astrophysics, the Las Cumbres Observatory Global Telescope Network Incorporated, the National Central University of Taiwan, the Space Telescope Science Institute, the National Aeronautics and Space Administration under Grant No. NNX08AR22G issued through the Planetary Science Division of the NASA Science Mission Directorate, the National Science Foundation under Grant No. AST-1238877, the University of Maryland, and Eotvos Lorand University (ELTE), the Los Alamos National Laboratory, and the Gordon and Betty Moore Foundation.

This paper makes use of software developed for the Large Synoptic Survey Telescope. We thank the LSST Project for making their code available as free software at http://dm.lsst.org.

This research made use of the following additional software: Astropy (Astropy Collaboration et al. 2013; Price-Whelan et al. 2018), matplotlib (Hunter 2007), and scipy(Virtanen et al. 2020), including numpy (van der Walt et al. 2011).

The authors wish to recognize and acknowledge the very significant cultural role and reverence that the summit of Mauna Kea has always had within the indigenous Hawaiian community. We are most fortunate to have the opportunity to conduct observations from this mountain.

REFERENCES

Astropy Collaboration, Robitaille, T. P., Tollerud, E. J., et al. 2013, A&A, 558, A33 6
Bañados, E., Venemans, B. P., Mazzucchelli, C., et al. 2018, Nature, 553, 473 1
Becker, G. D., Bolton, J. S., Madau, P., et al. 2015, MNRAS, 447, 3402 1, 2.1, 5.3
Becker, G. D., D'Aloisio, A., Christenson, H. M., et al. 2021, MNRAS, 508, 1853 5.1, 5.2
Becker, G. D., Davies, F. B., Furlanetto, S. R., et al. 2018, ApJ, 863, 92 1, 2.2, 3.1, 4, 5.1, 6, A
Becker, G. D., Pettini, M., Rafelski, M., et al. 2019, ApJ, 883, 163 2.1, 2.1, 15, B
Bertin, E., & Arnouts, S. 1996, A&AS, 117, 393 2.2
Boera, E., Becker, G. D., Bolton, J. S., & Nasir, F. 2019, ApJ, 872, 101 1
Bosman, S. E. I., Fan, X., Jiang, L., et al. 2018, MNRAS, 479, 1055 1, 5.3
Bosman, S. E. I., Davies, F. B., Becker, G. D., et al. 2021, arXiv e-prints, arXiv:2108.03699 1, 5.3
Bouwens, R. J., Illingworth, G. D., Oesch, P. A., et al. 2015, ApJ, 803, 34 5.1
Bruns, L. R., Wyithe, J. S. B., Bland-Hawthorn, J., & Dijkstra, M. 2012, MNRAS, 421, 2543 5.3
Chambers, K. C., Magnier, E. A., Metcalfe, N., et al. 2016, arXiv e-prints, arXiv:1612.05560 2.2
Chardin, J., Haehnelt, M. G., Aubert, D., & Puchwein, E. 2015, MNRAS, 453, 2943 1, 5.1, 8, 6
Chardin, J., Puchwein, E., & Haehnelt, M. G. 2017, MNRAS, 465, 3429 1, 5.1, 8, 6
Christenson, H. M., Becker, G. D., Furlanetto, S. R., et al. 2021, ApJ, 923, 87 1, 2.2, 3.1, 3.2, 4, 4, 5.1, 6, A, 17, D
Cooke, J., Omori, Y., & Ryan-Weber, E. V. 2013, MNRAS, 433, 2122 5.3
D'Aloisio, A., McQuinn, M., & Trac, H. 2015, ApJL, 813, L38 1, 5.1, 8, 6
D'Aloisio, A., Upton Sanderbeck, P. R., McQuinn, M., Trac, H., & Shapiro, P. R. 2017, MNRAS, 468, 4691 1
Davies, F. B., Becker, G. D., & Furlanetto, S. R. 2018a, ApJ, 860, 155 5.1, 5.3, 6
Davies, F. B., & Furlanetto, S. R. 2016, MNRAS, 460, 1328 1, 8
Davies, F. B., Hennawi, J. F., Bañados, E., et al. 2018b, ApJ, 864, 142 1
Dijkstra, M., & Wyithe, J. S. B. 2012, MNRAS, 419, 3181 5.1
Eilers, A.-C., Davies, F. B., & Hennawi, J. F. 2018, ApJ, 864, 53 1, 2.1, 5.3
Faisst, A. L., Chary, R. R., Fajardo-Acosta, S., et al. 2022, ApJ, 929, 66 1
Fan, X., Strauss, M. A., Becker, R. H., et al. 2006, AJ, 132, 117 1
Francis, P. J., & Bland-Hawthorn, J. 2004, Monthly Notices of the Royal Astronomical Society, 353, 301 5.3
Gaikwad, P., Rauch, M., Haehnelt, M. G., et al. 2020, MNRAS, 494, 5091 1
Garaldi, E., Compostella, M., & Porciani, C. 2019, MNRAS, 483, 5301 1
Garaldi, E., Kannan, R., Smith, A., et al. 2022, MNRAS, 512, 4909 5.2
Greig, B., Mesinger, A., & Bañados, E. 2019, MNRAS, 484, 5094 1
Greig, B., Mesinger, A., Haiman, Z., & Simcoe, R. A. 2017, MNRAS, 466, 4239 1
Huang, Y., Lee, K.-S., Cucciati, O., et al. 2022, ApJ, 941, 134 5.3
Hunter, J. D. 2007, Computing in Science & Engineering, 9, 90 6
Ishimoto, R., Kashikawa, N., Kashino, D., et al. 2022, MNRAS, 515, 5914 1, 2.1, 5.3, 11, 12, 13, 14, 6, 15, 4, B, B
Ivezić, v., Tyson, J. A., Acosta, E., et al. 2008, arXiv:0805.2366v4 2.2
Jung, I., Finkelstein, S. L., Dickinson, M., et al. 2020, ApJ, 904, 144 1
Jurić, M., Kantor, J., Lim, K., et al. 2015, ArXiv e-prints, arXiv:1512.07914 2.2
Kakiichi, K., Ellis, R. S., Laporte, N., et al. 2018, MNRAS, 479, 43 5.2
Kashikawa, N., Kitayama, T., Doi, M., et al. 2007, ApJ, 663, 765 5.3
Kashino, D., Lilly, S. J., Matthee, J., et al. 2023, ApJ, 950, 66 5.2, 5.3
Kashino, D., Lilly, S. J., Shibuya, T., Ouchi, M., & Kashikawa, N. 2020, ApJ, 888, 6 1, 5.3
Keating, L. C., Kulkarni, G., Haehnelt, M. G., Chardin, J., & Aubert, D. 2020a, MNRAS, 497, 906 1, 6
Keating, L. C., Weinberger, L. H., Kulkarni, G., et al. 2020b, MNRAS, 491, 1736 1, 5.3, 6
Konno, A., Ouchi, M., Shibuya, T., et al. 2017, Publications of the Astronomical Society of Japan, 70, s16 5, 4
Kulkarni, G., Worseck, G., & Hennawi, J. F. 2019, MNRAS, 488, 1035 1, 6
Li, Q., Wang, R., Fan, X., et al. 2023, arXiv e-prints, arXiv:2304.04719 5.3
Lidz, A., Oh, S. P., & Furlanetto, S. R. 2006, ApJL, 639, L47 1
López, S., D'Odorico, V., Ellison, S. L., et al. 2016, A&A, 594, A91 B
Mason, C. A., Treu, T., Dijkstra, M., et al. 2018, ApJ, 856, 2 1
McGreer, I. D., Fan, X., Jiang, L., & Cai, Z. 2018, AJ, 155, 131 1
Meyer, R. A., Bosman, S. E. I., Kakiichi, K., & Ellis, R. S. 2019, MNRAS, 483, 19 5.2
Meyer, R. A., Kakiichi, K., Bosman, S. E. I., et al. 2020, MNRAS, 494, 1560 5.2
Morales, A., Mason, C., Bruton, S., et al. 2021, arXiv e-prints, arXiv:2101.01205 1
Mortlock, D. J., Warren, S. J., Venemans, B. P., et al. 2011, Nature, 474, 616 1
Nasir, F., & D'Aloisio, A. 2020, MNRAS, 494, 3080 1, 5.1, 8, 5.2, 5.3, 12, 6
Ouchi, M., Shimasaku, K., Akiyama, M., et al. 2008, ApJS, 176, 301 3.2, 5, 4
Planck Collaboration, Aghanim, N., Akrami, Y., et al. 2020, A&A, 641, A6 1
Price-Whelan, A. M., Sipőcz, B. M., Günther, H. M., et al. 2018, AJ, 156, 123 6
Prochaska, J. 2017, Astronomy and Computing, 19, 27 15, B
van der Walt, S., Colbert, S. C., & Varoquaux, G. 2011, Computing in Science Engineering, 13, 22 6
Virtanen, P., Gommers, R., Oliphant, T. E., et al. 2020, Nature Methods, 17, 261 6
Wang, F., Davies, F. B., Yang, J., et al. 2020, ApJ, 896, 23 1
Wise, J. H. 2019, arXiv e-prints, arXiv:1907.06653 1
Yang, J., Wang, F., Fan, X., et al. 2020, ApJ, 904, 26 1, 5.3
Zhu, Y., Becker, G. D., Bosman, S. E. I., et al. 2021, arXiv:2109.06295 1, 2.1, 5.2, 13, 5.3, 15, B
Zhu, Y., Becker, G. D., Bosman, S. E. I., et al. 2022, ApJ, 932, 76 1, 15, B

APPENDIX

A. LYMAN-ALPHA OPACITY OF QUASAR SIGHTLINES

Following Becker et al. (2018); Christenson et al. (2021), we use our imaging data to estimate the Lyα effective opacity for the highly transmissive J1306 and J359 sightlines. Measurements made from the imaging data are comparable to spectroscopic measurements made over 28 h^{-1} Mpc centered on the NB0816 filter wavelengths, and represents an effective opacity measurement made over the width of the NB816 filter. The general procedure is as follows: for each quasar, we begin by measuring the NB816 and HSC-$i2$ fluxes from the imaging data following Section 3.1. We then convolve each quasar spectrum with the $i2$ transmission curve and scale them so that the transmission-weighted mean flux matches the $i2$ flux measured from the imaging data. We then estimate the unabsorbed continuum flux

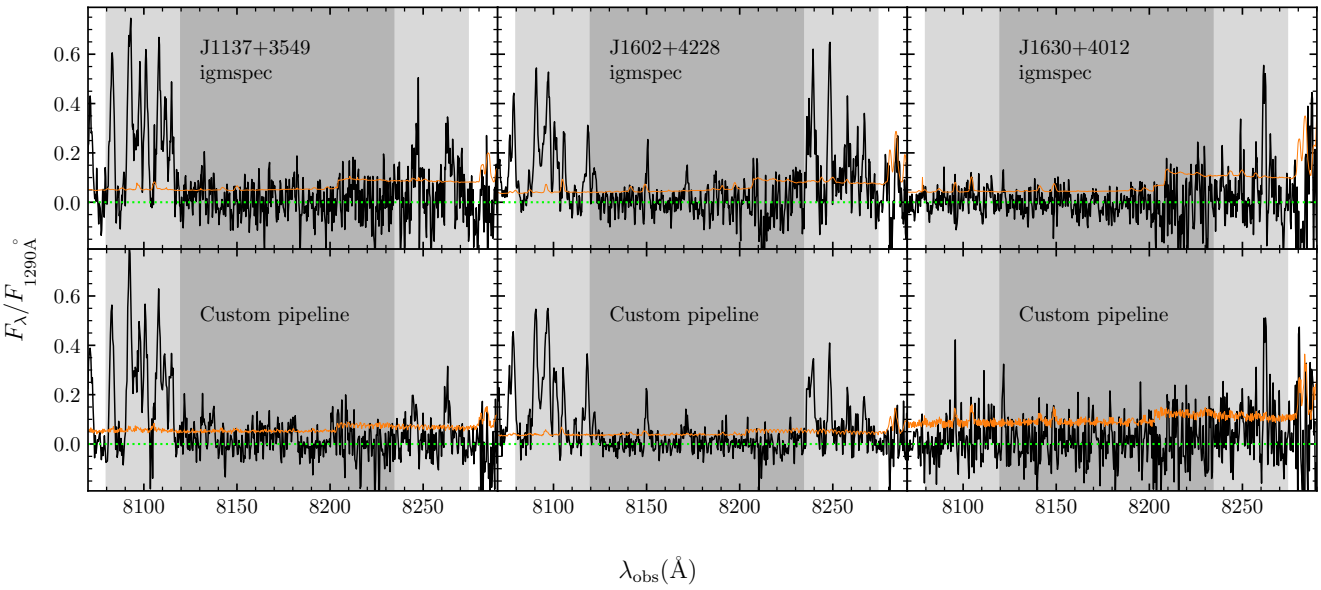

Figure 15. Partial spectra of quasars J1137+3549, J1602+4228, and J1630+4012 (left to right). The top panels show the spectra for these objects used by Ishimoto et al. (2022), which were selected from the `igmspec` database (Prochaska 2017). The bottom panels show reductions using a pipeline customized for high-redshift QSOs Becker et al. (e.g., 2019); Zhu et al. (e.g., 2021); Zhu et al. (e.g., 2022). The solid orange lines indicate the flux error and the green dotted line marks a flux of zero. The darker gray shaded rectangles indicate the FWHM of the NB816 filter, which corresponds to 28 h^{-1} Mpc and the lighter shaded regions indicate the 50 h^{-1} Mpc interval over which effective opacity measurements are made. The opacity measurements made from these spectra, both in this work and in Ishimoto et al. (2022), are summarized in Table 4.

expected at the Lyα wavelength from PCA fits for the blue-side continuum of each quasar spectrum. Combining these measurements, we calculate the effective opacity as $\tau_{\rm eff} = -\ln(\mathrm{F}_\lambda^{\rm NB816}/\mathrm{F}_\lambda^{\rm cont})$.

For the J1306 sightline, we measure $F_\lambda^{NB816} = (11.2\pm0.2)\times10^{-19}$ erg s^{-1} cm^{-2} Å^{-1} and $F_\lambda^{i2} = (28.3\pm0.2)\times10^{-19}$ erg s^{-1} cm^{-2} Å^{-1}, and estimate that the unabsorbed continuum is $F_\lambda^{\rm cont} \simeq 1.6\times10^{17}$ erg s^{-1} cm^{-2} Å^{-1}. We therefore measure $\tau_{\rm eff} = 2.64\pm0.02$. For comparison, we measure $\tau_{\rm eff}^{28} = 2.475\pm0.010$ from the X-Shooter spectrum. The uncertainty in $\tau_{\rm eff}$ is based on the propagated uncertainty in F_λ^{NB816} and does not account for uncertainty in the estimated continuum.

For the J359 sightline, we measure $F_\lambda^{NB816} = (9.7\pm0.2)\times10^{-19}$ erg s^{-1} cm^{-2} Å^{-1} and $F_\lambda^{i2} = (7.8\pm0.1)\times10^{-19}$ erg s^{-1} cm^{-2} Å^{-1}, and estimate that the unabsorbed continuum is $F_\lambda^{\rm cont} = 0.8\times10^{17}$ erg s^{-1} cm^{-2} Å^{-1}. We therefore measure $\tau_{\rm eff} = 2.26\pm0.02$. From the spectra, we measure $\tau_{\rm eff}^{28} = 2.338\pm0.01$ over the filter width. For both sightlines, if we assume a 20% uncertainty in the continuum, the uncertainty in our measurements from the imaging becomes ±0.09.

B. Lyα OPACITY MEASUREMENTS FOR ISHIMOTO ET AL. (2022) LINES OF SIGHT

Table 4
Effective opacity measurements for QSO sightlines Ishimoto et al. (2022)

QSO	$\tau_{\rm eff}^{50,a}$ (this work)	$\tau_{\rm eff}^{50,b}$ (Ishimoto et al. (2022))	$\tau_{\rm eff}^{28,c}$ (this work)	$\tau_{\rm eff}^{28,d}$ (Ishimoto et al. (2022))
SDSS J1137+3549	2.904 ± 0.042	3.07 ± 0.03	4.344 ± 0.227	5.58 ± 0.62
SDSS J1602+4228	3.063 ± 0.038	3.23 ± 0.05	4.898 ± 0.308	6.05 ± 0.91
SDSS J1630+4012	3.857 ± 0.184	5.47 ± 0.86	4.550 ± 0.477	$>5.06^e$

[a] Effective opacity used in this work, measured over a 50 h^{-1} Mpc window centered at 8177 Å
[b] Effective opacity from Ishimoto et al. (2022), measured over a 50 h^{-1} Mpc window centered at 8177 Å
[c] Effective opacity used in this work, measured over a 28 h^{-1} Mpc window centered at 8177 Å
[d] Effective opacity from Ishimoto et al. (2022), measured over a 30 h^{-1} Mpc window centered at 8177 Å
[e] Lower limit

In this work we use updated $\tau_{\rm eff}$ values for the three lines of sight included in Ishimoto et al. (2022). Ishimoto et al. (2022) used Keck ESI spectra from the publicly available `igmspec` database (Prochaska 2017). In contrast, we use versions of these data reduced using a custom pipeline that has been highly optimized for high-redshift QSO spectra (for a description of the pipeline, see López et al. 2016; Becker et al. 2019; Zhu et al. 2021). The custom reductions for all three were first presented in Becker et al. (2019), while J1137 and J1602 were also presented in Zhu et al. (2021);

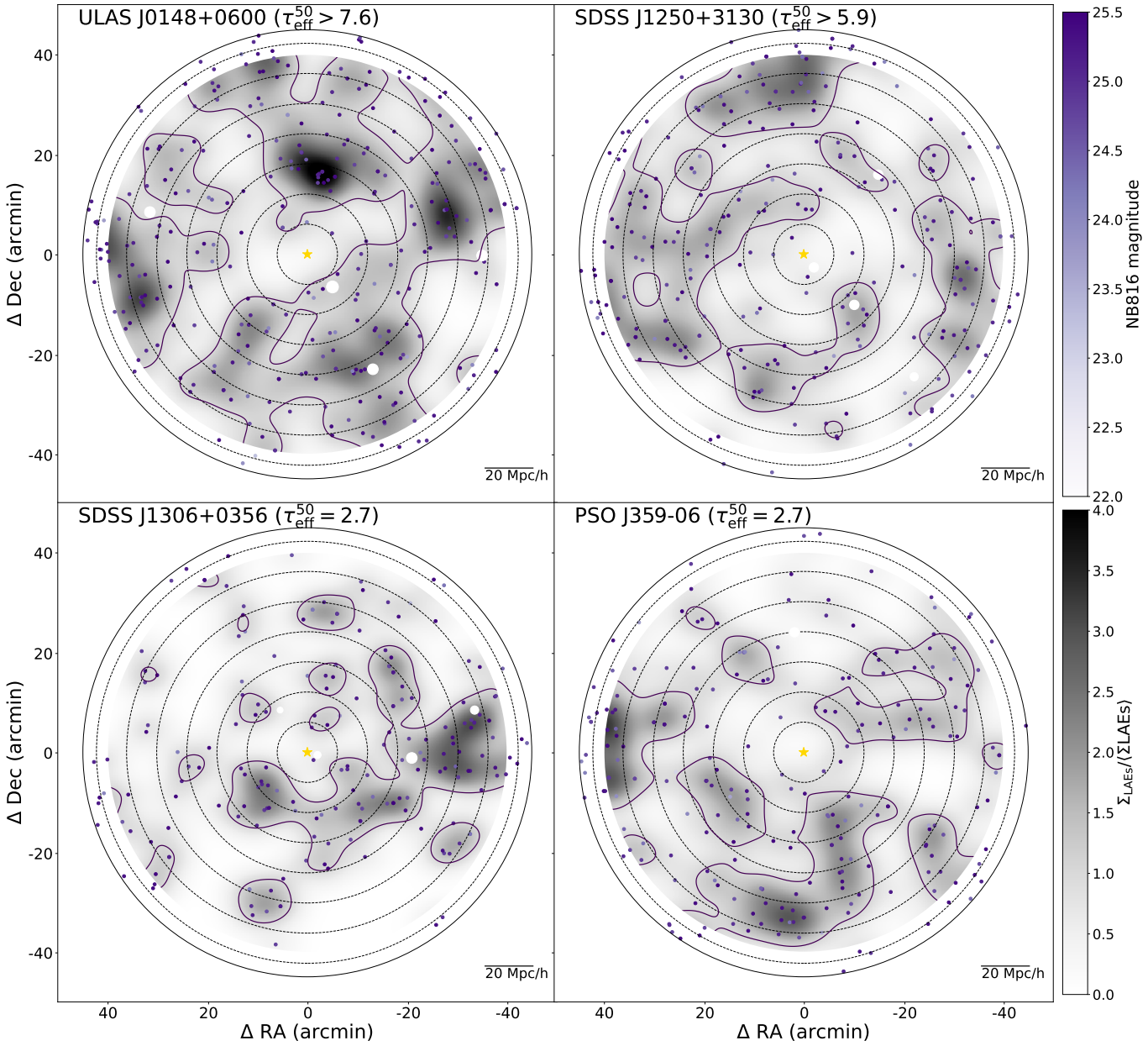

Figure 16. Distribution of LAE candidates in all four fields: J0148 (top left), J1250 (top right), J1306 (bottom left), and J359 (bottom right). The LAE candidates are assigned a color that indicates their NB816 magnitude. The grayscale shading in the background indicates the surface density of LAE candidates, which we calculate by kernel density estimation and normalized by the global mean surface density of all four fields, measured over $15' \leq \Delta\theta \leq 40'$. This surface density is corrected for spatial variations in completeness as described in Section 3.3. The field is centered on the quasar position, which is marked with a gold star, and the concentric dotted rings indicate 10 h^{-1} Mpc intervals from the quasar position. The solid ring marks the edge of the field, 45′ from the quasar position. Portions masked out of the field in white are obscured by foreground stars.

Zhu et al. (2022). Our measurements of $\tau_{\rm eff}$ over the two wavelength regions indicated in Figure 15, corresponding to 28 and 50 h^{-1} Mpc, are given in Table B, along with values from Ishimoto et al. (2022).

We find somewhat lower values of $\tau_{\rm eff}^{28}$ for J1137 and J1602, and a lower $\tau_{\rm eff}^{50}$ for J1630. For J1137, our reduction reveals transmission peaks near 8134 and 8180 Å. Taking the transmission from these peaks alone gives $\tau_{\rm eff}^{28} = 4.887 \pm 0.391$, which should be an upper limit on the effective opacity over the entire window as we are assuming that all other pixels have zero transmission. This value is consistent with our measurement in Table B. In the case of J1602, the higher $\tau_{\rm eff}^{2}8$ value in Ishimoto et al. (2022) is explained by the presence of a spurious negative feature near 8212 Å, which is not as strong in our reduction. Similarly, the `igmspec` reduction of J1630 appears to show a slight negative bias over 8160–8220 Å, which helps to explain the difference in the $\tau_{\rm eff}^{50}$ values.

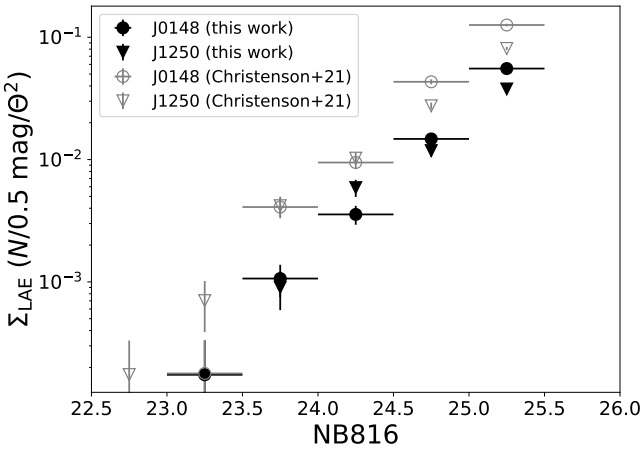

Figure 17. Completeness-corrected surface density of LAE candidates in the J0148 and J1250 fields in this work (filled markers) and Christenson et al. (2021) (open markers).

C. GLOBALLY NORMALIZED LAE MAPS

In Section 4, we present maps of the LAE candidates in the J0148, J1250, J1306, and J359 fields. Those maps are normalized by the mean surface density in each field, calculated over $15' \leq \Delta\theta \leq 40'$. Normalizing the maps in this way allows us to self-consistently compare the vicinity of the quasar sightline to the rest of the field and determine whether the center of the field is over- or underdense relative to its surroundings. This type of normalization is also useful for making comparisons between fields, as it mitigates differences in depth, seeing, and other observational considerations, and it is the normalization used for all figures in the main body of the text.

However, we can also use the four fields we have observed to date to estimate a global mean surface density and compare the four fields on an absolute scale. This global normalization is limited by the small number of fields observed to date, but is useful for considering how the environments of these four sightlines compare to each other. Figure 16 shows the LAE maps from Section 4. As previously, the fields are centered on the quasar position (yellow star), foreground stars are masked out in white, and the concentric dotted rings indicate 10 h^{-1} Mpc intervals. The purple shading indicates the NB816 magnitude of the LAEs, and the grayscale shading indicates the surface density of LAEs (see Section 4 for details of the calculation). The surface density is completeness corrected (see Section 3.3) and normalized by the global mean surface density, which we measure over the $15' \leq \theta \leq 40'$ region of all four fields.

On an absolute scale, all four sightlines are underdense within 10 h^{-1} Mpc of the quasar, consistent with the maps that are normalized individually (see Figure 6). However, we note that the J0148 field, while underdense in the vicinity of the quasar sightline, seems to reside in a higher density region overall than the other three fields.

D. COMPARISON TO CHRISTENSON ET AL. 2021 SELECTIONS

Here we compare the selections of LAEs made in the J0148 and J1250 fields in this work to those published in Christenson et al. (2021). In this work, we select 298 LAEs in the J0148 field and 247 in the J1250 field, compared to 641 in the J0148 field and 428 in the J1250 field in Christenson et al. (2021). We show the surface density as a function of $NB816$ magnitude for both selections in Figure 17, and refer the reader to Figures 6, 7, and the corresponding figures in Christenson et al. (2021) for a comparison of the LAE maps and radial surface density distributions. There are two primary differences between these catalogs. First, as discussed in Section 3.1, is the use of aperture fluxes as the primary photometric measurement in this work. Aperture fluxes are expected to have lower signal-to-noise compared to PSF fluxes and hence produce fewer detections. Second, we have made a more careful measurement of the seeing in this work, making use of bright stars selected to be bright, but not saturated, and the seeing tends to be slightly better than previously estimated. The PSF fluxes from Christenson et al. (2021), which are fit to a broader profile than the true extent of the sources, therefore tend to be higher than the aperture fluxes. For these two reasons, the measured surface density is not consistent between the two selections. We note that brightest objects consistently appear in both catalogs but tend to fall in fainter magnitude bins in this work, which is the reason for the poor agreement in the brighter magnitude bins. Despite these differences, the key results of Christenson et al. (2021) are unchanged in this work; both highly opaque sightlines display clear underdensities within 20 h^{-1} Mpc of the quasar sightline, and the large-scale structure of the field is consistent between the two selections.